

Transient and Equilibrium Responses of the Atlantic Overturning Circulation to Warming in Coupled Climate Models: The Role of Temperature and Salinity

DAVID B. BONAN,^a ANDREW F. THOMPSON,^a EMILY R. NEWSOM,^b SHANTONG SUN,^a AND MARIA RUGENSTEIN^c

^a *California Institute of Technology, Pasadena, California*

^b *University of Oxford, Oxford, United Kingdom*

^c *Colorado State University, Fort Collins, Colorado*

(Manuscript received 29 November 2021, in final form 6 April 2022)

ABSTRACT: The long-term response of the Atlantic meridional overturning circulation (AMOC) to climate change remains poorly understood, in part due to the computational expense associated with running atmosphere–ocean general circulation models (GCMs) to equilibrium. Here, we use a collection of millennial-length GCM simulations to examine the transient and equilibrium responses of the AMOC to an abrupt quadrupling of atmospheric carbon dioxide. We find that GCMs consistently simulate an AMOC weakening during the first century but exhibit diverse behaviors over longer time scales, showing different recovery levels. To explain the AMOC behavior, we use a thermal-wind expression, which links the overturning circulation to the meridional density difference between deep-water formation regions and the Atlantic basin. Using this expression, we attribute the evolution of the AMOC on different time scales to changes in temperature and salinity in distinct regions. The initial AMOC shoaling and weakening occurs on centennial time scales and is attributed to a warming of the deep-water formation region. A partial recovery of the AMOC occurs over the next few centuries, and is linked to a simultaneous warming of the Atlantic basin and a positive high-latitude salinity anomaly. The latter reduces the subsurface stratification and reinvigorates deep-water formation. GCMs that exhibit a prolonged AMOC weakening tend to have smaller high-latitude salinity anomalies and increased Arctic sea ice loss. After multiple millennia, the AMOC in some GCMs is stronger than the initial state due to warming of the low-latitude Atlantic. These results highlight the importance of considering high-latitude freshwater changes when examining the past and future evolution of the AMOC evolution on long time scales.

SIGNIFICANCE STATEMENT: The long-term response of the ocean’s global overturning circulation to warming remains poorly understood largely because it is expensive to run state-of-the-art climate models. This study makes use of a unique collection of millennial-length climate simulations from different climate models to examine the response of the Atlantic overturning circulation to warming on long time scales. We find that climate models consistently simulate a weakening of the Atlantic overturning circulation during the first century after warming, but disagree on long-term changes, showing different recovery levels of the Atlantic overturning circulation. Using a simple expression, which emulates the evolution of the Atlantic overturning circulation in climate models, we show that climate models with little to no recovery tend to have a small North Atlantic salinity anomaly while climate models with a stronger recovery tend to have a large North Atlantic salinity anomaly. These results highlight the importance of monitoring high-latitude freshwater sources throughout the twenty-first century and considering the relative role of temperature and salinity changes when examining the future and past evolution of the Atlantic overturning circulation on long time scales.

KEYWORDS: Ocean; Atmosphere–ocean interaction; Meridional overturning circulation; Ocean circulation; Thermocline circulation; Climate change; Climate models; General circulation models

1. Introduction

The ocean’s global overturning circulation plays a fundamental role in shaping Earth’s climate through the redistribution of heat and freshwater between low and high latitudes and different ocean basins. The branch of the overturning circulation that is localized to the Atlantic basin, referred to as the Atlantic meridional overturning circulation (AMOC), plays a unique role in that it transports heat northward across all latitudes (Ganachaud and Wunsch 2003) and ventilates the upper ~2000 m of the ocean (Buckley and Marshall 2016). The AMOC is frequently invoked as a major player in past

climatic changes (Broecker 1997, 1998, 2003; Ferrari et al. 2014) and is thought to play a large role in setting features of today’s climate, such as shifting the peak of tropical rainfall to the Northern Hemisphere (Frierson et al. 2013; Marshall et al. 2014; Buckley and Marshall 2016). Paleoclimate records, based on both $\delta^{13}\text{C}$ and Cd/Ca ratios in benthic foraminifera, suggest the AMOC was shallower and potentially weaker at the Last Glacial Maximum (LGM; Curry and Oppo 2005; Lynch-Stieglitz et al. 2007; Burke et al. 2015), although this is still debated as these proxies may better reflect changes in the distribution of nutrients (Gebbie 2014). Comprehensive general circulation models (GCMs) also indicate that the AMOC can exist in a range of configurations (Weber et al. 2007; Cheng et al. 2013; Weijer et al. 2020), yet a mechanistic understanding of how the AMOC transitions between these states

Corresponding author: David B. Bonan, dbonan@caltech.edu

DOI: 10.1175/JCLI-D-21-0912.1

© 2022 American Meteorological Society. For information regarding reuse of this content and general copyright information, consult the [AMS Copyright Policy](#) ([www.ametsoc.org/PUBSReuseLicenses](#)).

is less clear. In particular, there is no mechanistic understanding of what determines the time scales over which the AMOC might weaken and subsequently recover, and the relative importance of high- versus low-latitude processes in controlling these responses.

In response to increased greenhouse gas concentrations, GCMs consistently predict a weakening of the AMOC over the twenty-first century (Gregory et al. 2005; Weaver et al. 2007; Cheng et al. 2013; Kostov et al. 2014; Liu et al. 2020; Weijer et al. 2020). The weakening of the AMOC is thought to arise from a combination of increased freshwater fluxes and weakened surface heat loss in the North Atlantic (Dixon et al. 1999; Schmittner et al. 2005; Gregory et al. 2005; Stouffer et al. 2006; Weaver et al. 2007; Bakker et al. 2016; Maroon et al. 2018), both of which reduce the formation of North Atlantic Deep Water (NADW) through positive surface buoyancy flux anomalies. Advection of heat and salinity anomalies into the North Atlantic can also affect the AMOC by altering conditions that support deep convection and the depth to which NADW penetrates. For instance, studies have also attributed a weakening of the AMOC in GCMs to Arctic sea ice loss (Sévellec et al. 2017) and subsurface warming of the North Atlantic (Haskins et al. 2020; Levang and Schmitt 2020), which both increase ocean stratification and inhibit deep convection.

Beyond the twenty-first century, the response of the AMOC to rising greenhouse gas concentrations is less clear. From a logistical standpoint, the computational expense of running a GCM to equilibrium has limited the number of studies that consider millennial or longer time scales. Additionally, the few GCMs that have generated millennial-length climate simulations have produced divergent AMOC responses, including both recovered and collapsed states. For example, Manabe and Stouffer (1994) and Stouffer and Manabe (2003) found that in response to an abrupt increase in atmospheric carbon dioxide, the AMOC weakens initially and then recovers to its initial strength after approximately a thousand years. A similar long-term AMOC recovery, following an abrupt decrease in atmospheric carbon dioxide, was also identified in Stouffer and Manabe (2003). Other studies, which have focused only on changes to freshwater forcing, have also found similar recoveries of the AMOC on millennial time scales (Jackson 2013; Haskins et al. 2019). Yet, in some studies, the AMOC has remained in a weakened state for prolonged time periods (Stocker and Schmittner 1997; Liu et al. 2017; He et al. 2019) and taken much longer to fully recover (Stocker and Schmittner 1997; Wiebe and Weaver 1999; Rind et al. 2018; Thomas and Fedorov 2019). These studies do not provide a mechanistic explanation for the slower AMOC recovery or prolonged weakening states. There remains a pressing need to identify the mechanisms that lead to these divergent AMOC responses in GCMs on millennial time scales.

The complexities of coupled GCMs, however, make it challenging to identify individual mechanisms underpinning changes to the ocean's overturning circulation, which can arise from modification to the ocean's surface freshwater, heat, and momentum fluxes. Building on previous studies (e.g., Thorpe et al. 2001; de Boer et al. 2010; Butler et al. 2016; Haskins et al.

2019, 2020; Ragen et al. 2022), here we use the dynamic link between overturning strength and zonal/meridional density gradients in the Atlantic basin to attribute circulation anomalies to thermal and haline anomalies. This approach assumes that the response of the AMOC to forcing is sufficiently slow that it remains in geostrophic balance and the spatial structure of the overturning is related to the density distribution in the Atlantic basin through a thermal wind relationship. An advantage of this approach is that changes in the AMOC can be attributed to specific processes that modify the density field in various regions. For instance, in the hosing experiments by Haskins et al. (2019), the initial AMOC weakening is attributed to changes in the density localized to the high-latitude North Atlantic, while the recovery is attributed to density changes occurring in the low latitudes of the Atlantic basin. However, assessing changes to the AMOC from meridional density gradients alone has limitations (e.g., de Boer et al. 2010), and can be subject to misinterpretation when not accounting for changes to the AMOC depth that may be associated with changes in wind stress (Muglia and Schmittner 2015) or deep-ocean water masses (Sun et al. 2020a).

Connecting the ocean's density structure to overturning strength has been a key component of many idealized theoretical studies that have considered the response of the AMOC to various external forcing (Nikurashin and Vallis 2012; Jansen et al. 2018; Jansen and Nadeau 2019; Nadeau and Jansen 2020). Specifically, Jansen et al. (2018) and Jansen and Nadeau (2019) showed that the thermal wind relationship in an Atlantic-like basin is able to emulate the response of the ocean's overturning in an ocean-only simulation and is useful when mechanistically interpreting simulated overturning changes to atmospheric warming. Yet, these idealized models often neglect more sophisticated processes of the climate system that may substantially influence the AMOC. For instance, most conceptual models make assumptions about ocean-atmosphere coupling by either prescribing the isopycnal overturning circulation in the North Atlantic or neglecting interactions between the surface buoyancy forcing and overturning in the North Atlantic (Nikurashin and Vallis 2012; Jansen et al. 2018; Jansen and Nadeau 2019; Thomas and Fedorov 2019). Both of these approaches raise questions about the role of ocean-atmosphere interactions and the role of local North Atlantic versus remote lower-latitude changes in the response of the AMOC to external forcing. While these idealized models have improved our fundamental understanding of the AMOC dynamics, the long-term behavior of the AMOC in more complex coupled GCMs remains unclear. In particular, there is no widely agreed upon explanation for why GCMs produce both recovered and prolonged weakened AMOC states, despite being given the same greenhouse gas forcing.

In this study, we introduce a framework to examine processes influencing the transient and equilibrium responses of the AMOC to warming in coupled GCMs. To do this, we use a collection of millennial-length climate simulations in which the atmospheric carbon dioxide was abruptly quadrupled above preindustrial levels and held constant for the remainder of the simulation ($4 \times \text{CO}_2$), compiled as part of LongRunMIP

TABLE 1. Overview of each simulation. The resolution of the atmosphere and ocean is given in number of grid points as a function of latitude \times longitude \times depth. The last column contains references that describe the GCMs and simulations in more detail. Note that some simulations are the extensions of simulations discussed in the references.

Model name	Length (yr)	Atmosphere resolution	Ocean resolution	Reference
CESM1	5900	96×144	$384 \times 320 \times 60$	Rugenstein et al. (2016a)
CNRM-CM6.1	1850	128×256	$180 \times 360 \times 75$	Saint-Martin et al. (2019)
GISS-E2-R	5000	90×144	$180 \times 288 \times 32$	Schmidt et al. (2014)
HadGEM2-ES	1295	145×192	$216 \times 360 \times 40$	Andrews et al. (2015)
IPSL-CM5A-LR	1000	96×96	$149 \times 182 \times 31$	Dufresne et al. (2013)
MPI-ESM1.1	4458	96×192	$220 \times 256 \times 40$	Mauritsen et al. (2019)
MPI-ESM1.2	1000	96×192	$220 \times 256 \times 40$	Mauritsen et al. (2019)

(Rugenstein et al. 2019). A key asset of LongRunMIP is that it contains a diverse set of GCMs that exhibit strikingly different behaviors in response to $4 \times \text{CO}_2$, specifically in ocean properties (Frölicher et al. 2020; Rugenstein et al. 2019, 2020). Thus, this suite of GCM simulations provides a unique opportunity to identify processes governing the long-term evolution of the AMOC without the temporal limitations normally imposed by computational constraints. In what follows, we first show that the time evolution of the AMOC in GCMs can be well approximated by a thermal wind expression that relates the overturning circulation in the North Atlantic to the density difference between the region of deep-water formation and the Atlantic basin. Using this expression, we isolate thermal and haline contributions to changes in the time-dependent stratification in different regions of the Atlantic basin, and thus the circulation responses. From this approach, key controls on the level and time scale of AMOC recoveries are summarized and discussed.

2. Materials and methods

a. Model output and diagnostics

LongRunMIP is a model intercomparison project that aims to better understand centennial and millennial time scale atmosphere–ocean processes in coupled GCMs (Rugenstein et al. 2019). In this study, we limit our analysis to $4 \times \text{CO}_2$ simulations from seven different GCMs that span 1000 years or longer. A summary of the GCMs, including the length of each simulation, the resolution of the atmosphere and ocean components, and the relevant reference for further details are provided in Table 1. The GCM with the longest simulation is CESM1, which is run for 5900 years, and the GCMs with the shortest simulations are IPSL-CM5A-LR and MPI-ESM1.2, which are both run for 1000 years.

We focus on the evolution of the meridional overturning streamfunction in the Atlantic basin, which is provided in the LongRunMIP repository (given by the name “moc”). The overturning is archived as the meridional overturning circulation streamfunction, which is calculated as

$$\psi(t, y, z) = - \int_{-H}^z \int_{x_w}^{x_e} v(t, x, y, z) dx dz, \quad (1)$$

where t is time, x is longitudinal displacement, y is latitudinal displacement, z is depth with H being the depth of the ocean bottom, v is the total meridional velocity (including the eddy-

bolus contribution due to parameterized mesoscale eddies), and x_w and x_e are the western and eastern boundaries of the Atlantic basin. In the analyses below, the AMOC strength is defined as the maximum value of the meridional streamfunction in the North Atlantic, between 40° and 60°N .

To provide a more mechanistic interpretation of the AMOC responses in each GCM, we relate the overturning circulation in the North Atlantic to the density difference between the region of deep-water formation ρ_n and the Atlantic basin ρ_b . Density gradients have been widely used to understand controls on overturning strength in a number of theoretical studies (e.g., Stommel 1961; Welander 1971; Gnanadesikan 1999; Wolfe and Cessi 2010; Nikurashin and Vallis 2012; Jansen et al. 2018; Jansen and Nadeau 2019), and they also have been used to interpret the behavior of coupled GCMs (see references in section 1). We use potential density ρ referenced to the surface, calculated from the model-archived potential temperature (“theta”), and practical salinity (“so”). Note that we convert the respective fields to conservative temperature and absolute salinity. To attribute variations in the density field to thermal and haline changes, we use a linear equation of state with time- and depth-varying coefficients of thermal expansion α and haline contraction β , which can be expressed as

$$\rho(t, z) \approx \rho_0 \left\{ \underbrace{1 - \bar{\alpha}(t, z)[T(t, z) - T_0]}_{\text{thermal}} + \underbrace{\bar{\beta}(t, z)[S(t, z) - S_0]}_{\text{haline}} \right\}, \quad (2)$$

where ρ_0 is a reference potential density, T_0 is a reference temperature, and S_0 is a reference salinity. The coefficients $\bar{\alpha}$ and $\bar{\beta}$ are computed individually for each GCM and at each time step as a function of depth throughout the entire Atlantic basin (30°S – 60°N) using TEOS-10 (McDougall and Barker 2011). The reference values, ρ_0 , T_0 , and S_0 , are area-weighted and depth-averaged values for the Atlantic basin, calculated separately for each GCM, during years 1–10. The potential density of the North Atlantic ρ_n is computed using conservative temperature and absolute salinity averaged in zonal and meridional directions at each depth between 40° and 60°N . The potential density of the Atlantic basin ρ_b is computed using conservative temperature and absolute salinity averaged in zonal and meridional directions at each depth in the Atlantic basin between 30°S and 60°N . The sensitivity of the results to these exact domains is discussed in section 3b. A linear

equation of state is chosen for its ease in partitioning density changes into thermal and haline contributions. Below we show that density changes based on the linear equation of state recover the diagnosed overturning changes from each GCM. As discussed later, overturning circulation changes are mainly attributed to density changes in the upper 2000 m. Using potential density referenced to 1000 m, rather than the surface, does not qualitatively impact the results of this study.

We use the net surface heat flux (including those from ice formation and melting processes), freshwater flux (including precipitation, evaporation, runoff, melt from sea ice, frazil ice processes, salt flux from ocean-ice processes), sea surface salinity (“sos”), and sea surface temperature (“tos”) to calculate surface-forced water mass transformation (Walin 1982) for those GCMs that provided the necessary output (only CESM1 and CNRM-CM6.1). Finally, we use sea ice concentration (“sic”) to compute Arctic sea ice area, which is the sum of the percentage of sea ice in each grid cell multiplied by the grid cell area. In the analyses below, all variables are annual means computed from monthly output and smoothed with a Savitzky–Golay filter with a window size of 11 years. All anomalies are calculated relative to an average of years 1–10 because some GCMs do not provide output from the control run, from which the $4 \times \text{CO}_2$ simulations are initialized.

b. Interpretation of the simulated Atlantic overturning circulation

Following Nikurashin and Vallis (2012) and Jansen et al. (2018), we relate the meridional overturning circulation ψ in the northern part of the Atlantic basin to the density difference between the deep-water formation region and the whole Atlantic basin as

$$\frac{\partial^2 \psi}{\partial z^2} = -\frac{g}{\rho_0 f} (\rho_n - \rho_b), \quad (3)$$

where g is the gravitational acceleration (9.81 m s^{-2}), ρ_0 is a reference density (1025 kg m^{-3}), f is the Coriolis parameter around 60°N ($f = 1.2 \times 10^{-4} \text{ s}^{-1}$), and ψ is the meridional overturning transport streamfunction ($\text{m}^3 \text{ s}^{-1}$). Throughout this study, Eq. (3), which we will subsequently refer to as the TWR (thermal wind relationship), is solved with the boundary conditions, $\psi = 0$ at the surface and bottom of the ocean.

The TWR, as expressed in Eq. (3), relates zonal transport to a meridional density difference. A key assumption of this study is that in geostrophic balance, the meridional overturning transport and the zonal overturning transport are equivalent through continuity. In other words, a vertically sheared zonal flow at midlatitudes is connected to the depth–latitude overturning in the North Atlantic, a relationship that was proposed by Nikurashin and Vallis (2012). To our knowledge, this expression has not been tested in realistic GCM simulations and it is not obvious whether this expression will emulate the GCMs discussed in this study. As discussed in section 3, the TWR approximately captures the mean overturning strength as well as its temporal evolution. Differences between the streamfunction diagnosed from GCMs and the streamfunction diagnosed from TWR may result from the choice of the

averaging region to obtain ρ_n , which is discussed in more detail in section 3b.

3. Response of the Atlantic overturning circulation to abrupt forcing

In response to $4 \times \text{CO}_2$, the LongRunMIP GCMs show a relatively uniform response on centennial and shorter time scales, encompassing the weakening of the AMOC, but exhibit more diverse responses on long time scales during which the AMOC recovers at various rates. In the following subsections, we summarize key features of the long-term AMOC evolution, and then demonstrate that the TWR presented in Eq. (3) provides a suitable framework for understanding these AMOC changes.

a. Model response

The response of the AMOC to $4 \times \text{CO}_2$ in each GCM is first examined using the maximum value of the meridional streamfunction in the North Atlantic, defined between 40° and 60°N . All of the GCMs exhibit a weakening of the AMOC over centennial time scales (Fig. 1). GCMs with a stronger initial AMOC strength typically exhibit a larger AMOC weakening (Weijer et al. 2020), defined as a change in volume transport, with changes spanning 12 and 20 Sv ($1 \text{ Sv} \equiv 1 \times 10^6 \text{ m}^3 \text{ s}^{-1}$; Fig. 1c). GCMs with a weaker initial AMOC strength still experience substantial changes, but only weaken between 5 and 7 Sv (Fig. 1e). After the initial weakening of the AMOC, nearly all the GCMs (except for CNRM-CM6.1) exhibit a sustained strengthening of the AMOC, although the rate of this strengthening varies across the GCMs (Fig. 1h). In these GCMs, at least a partial recovery of the AMOC occurs, and in some cases the AMOC strength surpasses its initial magnitude, although this occurs over different time scales (Fig. 1h). In CESM1, for instance, the AMOC reaches 75% of its original strength around 300 years after the abrupt forcing, while in HadGEM2-ES the AMOC only recovers to 25% of its initial strength after approximately 1300 years (Fig. 1h). In CNRM-CM6.1, the AMOC weakens to approximately 2 Sv and remains weakened until around 1000 years, where it begins a slow, gradual recovery (Fig. 1b). Notably, approximately 3000 years after the abrupt forcing, the AMOC strength in CESM1, GISS-E2-R, and MPI-ESM1.1 is slightly stronger than their initial states by approximately 1–3 Sv (Fig. 1h). At the end of each simulation, some GCMs have reached a new steady state, whereas others are still evolving. However, the AMOC in all GCMs has either recovered or exhibits a gradual recovery.

In addition to changes in the AMOC strength, the vertical structure of the AMOC also evolves in response to $4 \times \text{CO}_2$. We examine the vertical structure of the AMOC in the North Atlantic as a function of time by calculating the maximum value of the meridional streamfunction at each depth between 40° and 60°N . All GCMs exhibit a shoaling of the AMOC depth, defined as the lower boundary of the overturning cell where $\psi = 0$ (see black line in Fig. 2), during the period of AMOC weakening on centennial time scales (Fig. 2). In contrast, the depth of the maximum value of the AMOC is relatively unchanged in response to increased greenhouse gas concentrations. However, the magnitude of shoaling in the

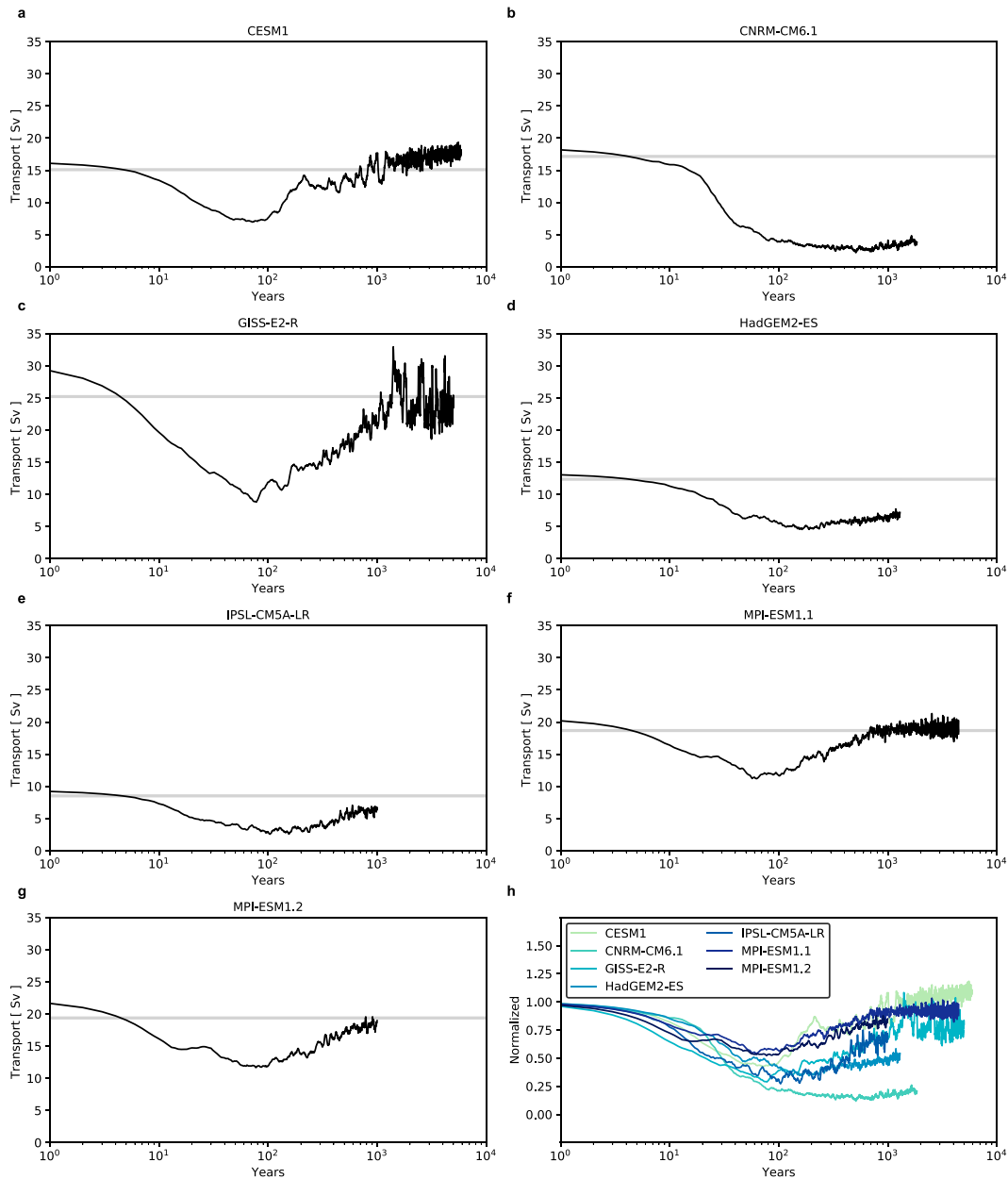


FIG. 1. Maximum value of the meridional streamfunction [Eq. (1)] between 40° and 60°N in the Atlantic basin from $4 \times \text{CO}_2$ simulations in (a) CESM1, (b) CNRM-CM6.1, (c) GISS-E2-R, (d) HadGEM2-ES, (e) IPSL-CM5A-LR, (f) MPI-ESM1.1, and (g) MPI-ESM1.2. (h) AMOC strength normalized by the initial strength (years 1–10) for each GCM. A Savitzky–Golay filter with a window size of 11 years was applied to each time series. In (a)–(g) the gray line denotes the initial strength (years 1–10).

AMOC depth varies substantially across the GCMs (black line in Fig. 2). In CNRM-CM6.1 the AMOC shoals by approximately 2000 m (Fig. 2b), whereas in MPI-ESM1.1 the AMOC shoals by approximately 500 m (Fig. 2f). In all GCMs except CNRM-CM6.1, the AMOC recovers in strength and deepens over the next millennia. In CESM1, GISS-E2-R, MPI-ESM1.1, and MPI-ESM1.2, the AMOC is eventually stronger than its initial state between 500 and 1000 m, but remains weakened below 1000 m (Fig. 2). After approximately 3000 years,

the AMOC deepens back to its initial depth in GISS-E2-R, MPI-ESM1.1, and MPI-ESM1.2, but not in CESM1, HadGEM2-ES, or IPSL-CM5A-LR. In CNRM-CM6.1, the AMOC stays weakened and remains shoaled by approximately 2000 m, even 1000 years after the $4 \times \text{CO}_2$ (Fig. 2b).

b. Validation of the thermal wind relationship

To better understand how the AMOC responses described in the previous section arise, we first examine the ability of

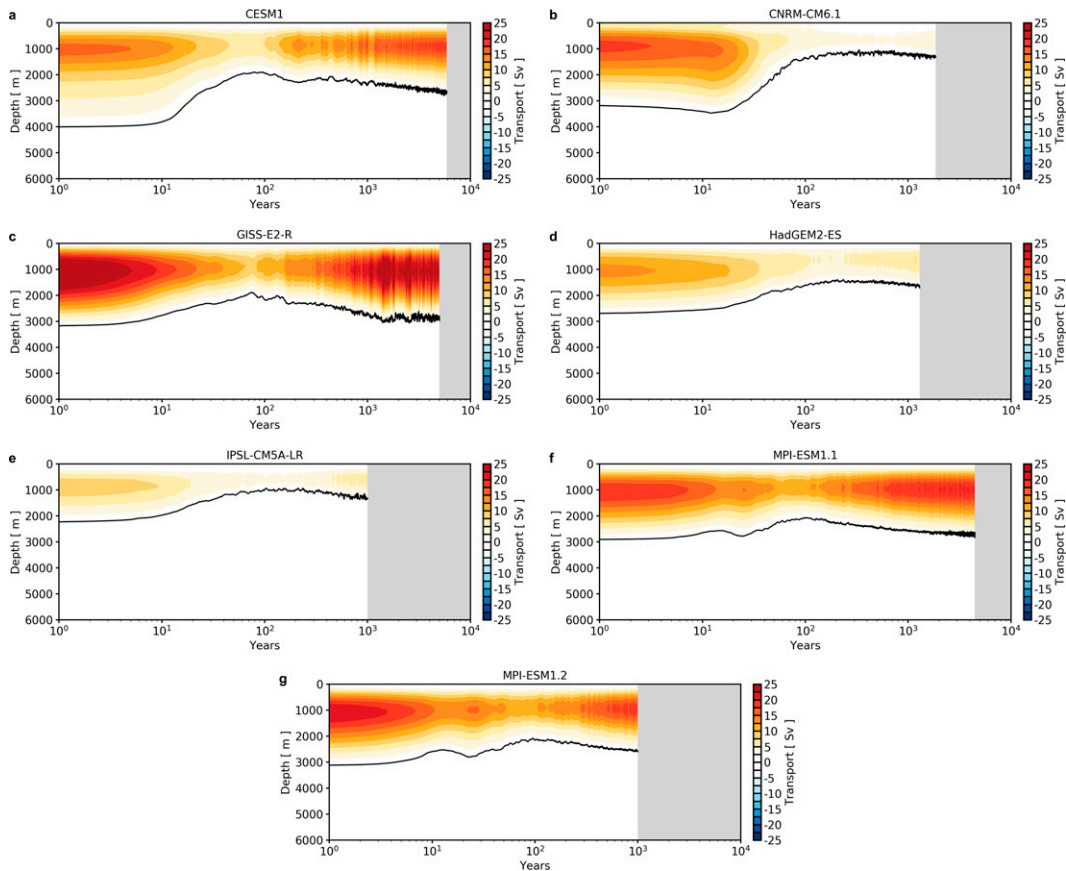


FIG. 2. Hovmöller plot of the maximum value of the meridional streamfunction [Eq. (1)] between 40° and 60° N in the Atlantic basin as a function of depth from $4 \times \text{CO}_2$ simulations in (a) CESM1, (b) CNRM-CM6.1, (c) GISS-E2-R, (d) HadGEM2-ES, (e) IPSL-CM5A-LR, (f) MPI-ESM1.1, and (g) MPI-ESM1.2. A Savitzky–Golay filter with a window size of 11 years was applied to each time series. The black line denotes where $\psi = 0$.

the TWR in Eq. (3) to emulate the AMOC responses in each GCM across a range of time scales. We compute spatially averaged potential density profiles in the North Atlantic and the entire Atlantic basin for each GCM (see section 2), and then apply the TWR in Eq. (3) to recreate the time-dependent overturning circulation in the North Atlantic. The results presented below are insensitive to the exact averaging choice of Atlantic basin domain, so long as estimates of ρ_b include the Atlantic basin northward of 30°S and estimates of ρ_n incorporates deep water formation regions, which also correspond to the location where the middepth isopycnals outcrop (Figs. 3a,b).

The meridional density difference, $\rho_n - \rho_b$, is largest near the surface and decreases to approximately zero around 1500–2000 m in most GCMs (Fig. 3c). The vertical structure and magnitude of the streamfunction computed from the TWR largely reproduces the streamfunction diagnosed from CESM1 (Fig. 3d). Note that the streamfunction below approximately 2000 m is overestimated by the TWR for CESM1 and most GCMs (not shown). More importantly, the maximum value of the overturning derived from the TWR approximates the time evolution of the AMOC for all GCMs. We provide one example of this agreement for CESM1 (Fig. 4a);

the other GCMs are similar. The TWR captures the initial weakening, partial recovery, and gradual restrengthening of the AMOC, although the TWR tends to underestimate the weakening of the AMOC in most GCMs.

To more quantitatively assess the skill of the TWR in reproducing the temporal evolution of the AMOC in each GCM, we compute a linear trend in the maximum value of the streamfunction across four different 150-yr time periods (years 0–150, years 200–350, years 450–600, and years 750–900) that span common years of each simulation. During the initial weakening (years 0–150), the TWR captures the simulated robust negative AMOC trends, but underestimates the magnitude, which spans -7 to -1 Sv century $^{-1}$ (Fig. 4a). This underestimation may come about because of the nontrivial relationship between surface-forced water mass transformation, interior stratification, and zonal and meridional overturning on centennial time scales (see section 5a). Nevertheless, the TWR accounts for approximately 50% of the intermodel variance. Importantly, the TWR captures much the general AMOC trends of each GCM. A comparison of the linear AMOC trend diagnosed from each GCM and the TWR across three time periods after the initial weakening (years 200–350,

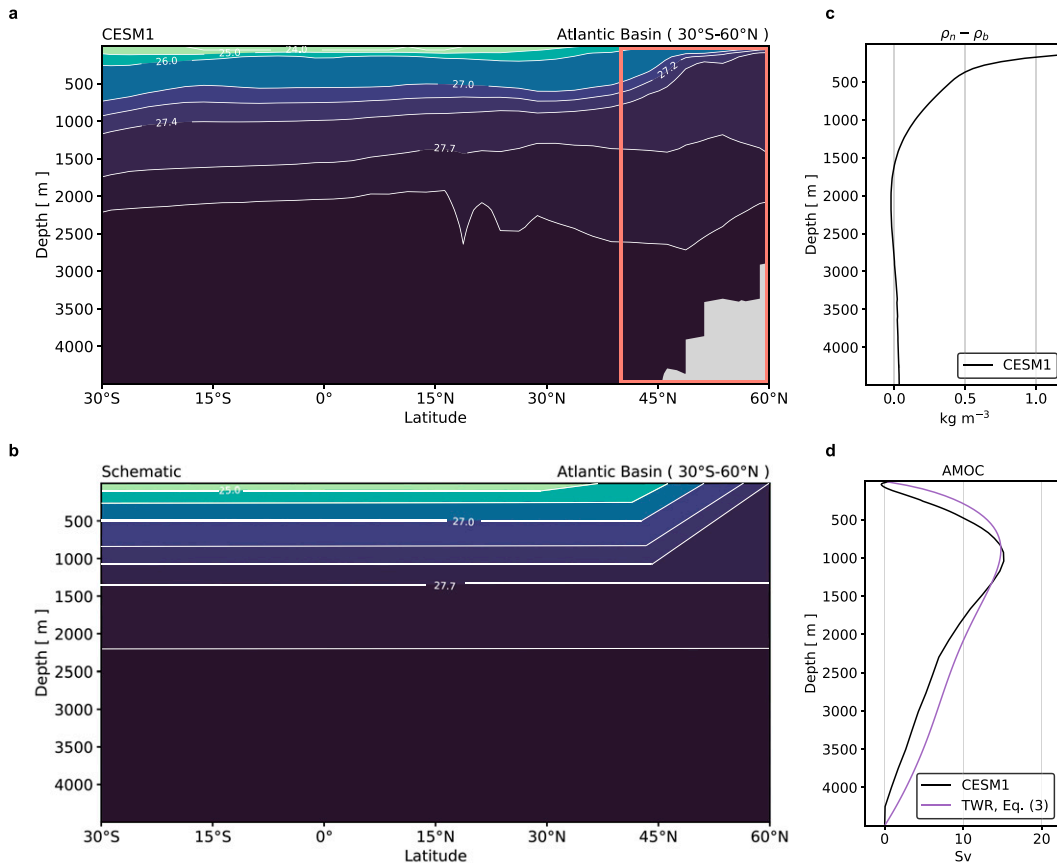


FIG. 3. Schematic showing how the thermal wind expression, Eq. (3), is applied to the LongRunMIP simulations. (a) Meridional section of isopycnals averaged zonally across the Atlantic basin during years 1–10 for CESM1. The red box denotes the averaging region for ρ_n , which is the same for all GCMs. (b) Schematic of the isopycnals in the Atlantic basin, which remain relatively flat throughout most of the basin and outcrop in the North Atlantic. (c) Density difference ($\rho_n - \rho_b$) between the density profile in the North Atlantic (40°–60°N) ρ_n and in the Atlantic basin (30°S–60°N) ρ_b in CESM1 during years 1–10. (d) The meridional streamfunction reported by CESM1 (black) and estimated from the meridional density difference in (c) with the thermal wind relationship, Eq. (3) (purple).

years 450–600, and years 750–900) shows that the TWR emulates the AMOC evolution during other time periods (Figs 4b–d). For each period, the TWR accounts for 50%–90% of the intermodel variance and also captures the broad tendency of a slow AMOC recovery in each GCM. The TWR also captures the shoaling of the AMOC during its weakening phase and the gradual deepening of the AMOC (not shown). The most significant deviation between overturning rates derived from Eq. (1) and the TWR occurs during the initial weakening phase of the AMOC. In the following, we use the TWR to examine drivers of the AMOC responses in each GCM, which can be attributed to density changes in the high-latitude North Atlantic (ρ_n) or throughout the Atlantic basin (ρ_b).

4. Thermal and haline controls on changes to the Atlantic overturning circulation

We next focus on changes to ρ_n , ρ_b , and $\rho_n - \rho_b$ since the Atlantic density distribution is coupled to the strength and

structure of the AMOC. In the analyses below, the symbol Δ indicates a change with respect to the initial state. Density changes are partitioned into thermal and haline contributions for three time periods that highlight different states of the AMOC evolution: the initial weakening phase, the partial recovery phase, and the restrengthening phase. The initial weakening phase is identified as a 30-yr average centered on the first local minimum of the AMOC magnitude for each model (see Fig. 1). The initial weakening phase spans slightly different years in the various GCMs, but it generally occurs within 50 years of the abrupt forcing (see Table 2). The partial recovery phase is chosen to be years 470–500, a period when the AMOC is increasing in most GCMs. Finally, the restrengthening phase is chosen to cover years 970–1000, a period of common years across all GCMs that occurs long after the abrupt forcing. Because some GCMs provide longer simulations than others, we also consider the new equilibrium state after multiple millennia (years 3500–3530) in the CESM1, GISS-E2-R, and MPI-ESM1.1 simulations.

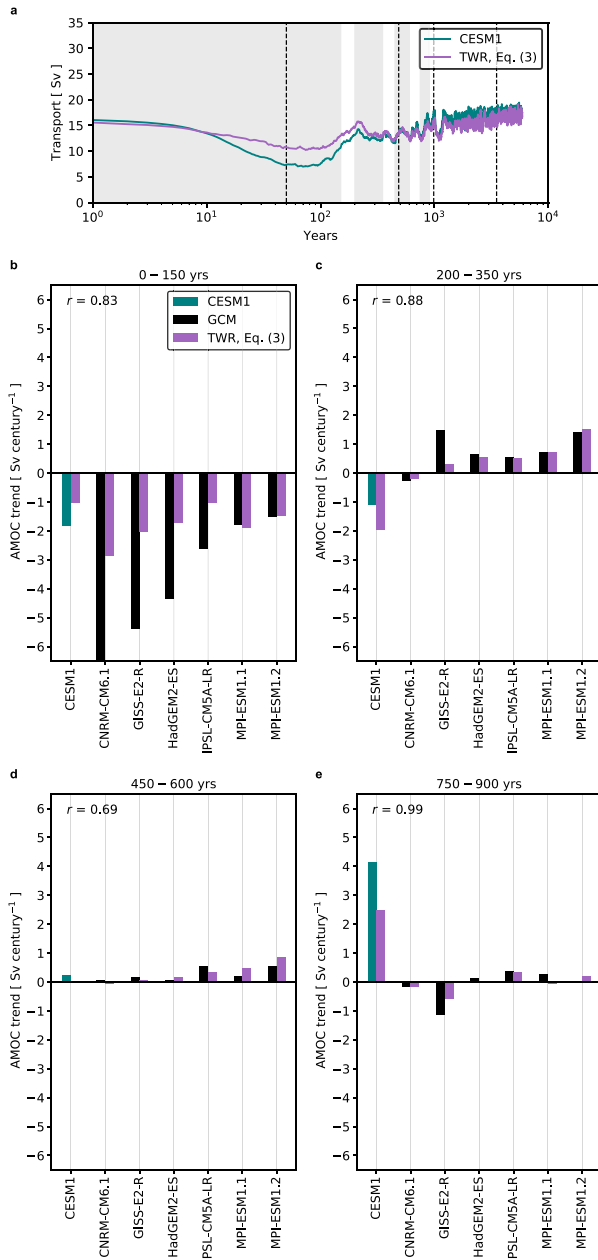


FIG. 4. Comparison of the AMOC changes calculated from GCMs and the thermal wind relationship in Eq. (3). (a) Maximum value of the meridional streamfunction between 40° and 60° N from Eq. (1) (teal) and Eq. (3) (purple) for CESM1. Linear trend of the maximum value of the meridional streamfunction between 40° and 60° N in the Atlantic basin from (b) 0–150, (c) 200–350, (d) 450–600, (e) 750–900 years for GCMs (black) and Eq. (3) (purple). The black dashed lines denote the average time periods examined in section 4. The gray shaded regions in (a) denote the periods for the linear trends. For (b)–(e) r is the Pearson correlation coefficient between the black and purple bars.

a. The initial weakening phase

During the initial weakening phase of the AMOC, $\Delta(\rho_n - \rho_b) < 0$ for all of the GCMs, indicating a weakening of the meridional density difference (Fig. 5a). The density difference decreases

TABLE 2. Time scale of the initial AMOC weakening in each GCM. The time scale is estimated as the first local minimum of the time series in Fig. 1.

Model name	Time scale (yr)
CESM1	48
CNRM-CM6.1	45
GISS-E2-R	29
HadGEM2-ES	40
IPSL-CM5A-LR	24
MPI-ESM1.1	21
MPI-ESM1.2	22

by 0.01 – 0.06 kg m^{-3} between 250 and 2000 m (Fig. 5a). The decrease in the basinwide density contrast for each GCM is almost entirely thermally driven (cf. red bar and blue bar), with the haline contribution actually increasing the basinwide density gradient in most GCMs (Fig. 5a). The weakening of $\rho_n - \rho_b$ across all GCMs results in a universal weakening and shoaling of the AMOC of approximately 1–6 Sv. GCMs with larger negative values of $\Delta(\rho_n - \rho_b)$ also show a greater weakening of the AMOC streamfunction (Fig. 5a).

Both $\Delta\rho_n$ and $\Delta\rho_b$ are negative during the initial weakening phase, indicating large-scale lightening of density throughout the Atlantic basin (Figs. 5b,c). In both regions this change is dominated by warming (the thermal contribution) with magnitudes that are roughly twice the size of $\Delta(\rho_n - \rho_b)$. However, changes to ρ_n exceed the changes to ρ_b due to warming during this initial weakening phase (i.e., $|\Delta\rho_n| > |\Delta\rho_b|$), which gives rise to the reduced meridional density difference. Salinity changes are weaker than and mostly oppose the thermal changes. GCMs with larger AMOC reductions (CNRM-CM6.1) tend to warm more in the North Atlantic, while GCMs with smaller AMOC reductions (IPSL-CM5A-LR and MPI-ESM1.1) tend to warm less in the North Atlantic.

b. The partial recovery phase

After the initial weakening, GCMs exhibit a much broader range of intermodel variability. About 500 years after the abrupt forcing, the AMOC in CESM1 recovers to approximately 90% of its initial strength, whereas the AMOC in CNRM-CM6.1 remains weakened to 15% of its initial strength (Fig. 1h).

During years 470–500, a majority of the GCMs still show that $\Delta(\rho_n - \rho_b) < 0$, but the values are less negative when compared to the initial weakening phase, indicating a slight increase in the meridional density difference relative to the weakened state (Fig. 6a). In MPI-ESM1.1 and MPI-ESM1.2, $\Delta(\rho_n - \rho_b) < 0$, indicating a stronger meridional density difference and a stronger AMOC when compared to the initial state (Fig. 6a). In most GCMs, the AMOC partially recovers by 1–3 Sv. In CNRM-CM6.1, however, $\rho_n - \rho_b$ further decreases and the anomaly becomes more negative when compared to the initial weakening phase. Note that the thermal contribution to $\Delta(\rho_n - \rho_b)$ now acts to increase the meridional density difference, which is the opposite of the weakening phase.

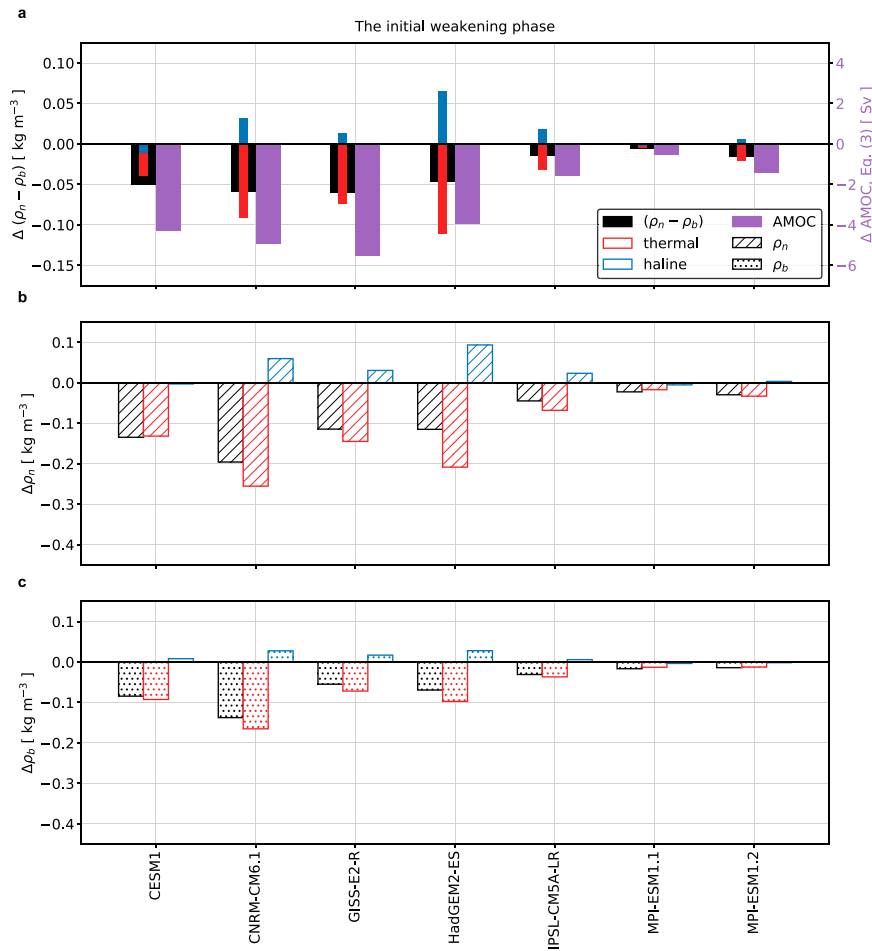


FIG. 5. (a) Bar plot showing the average density change between 250 and 2000 m for $(\rho_n - \rho_b)$ (black) and the maximal change in the meridional overturning circulation streamfunction using Eq. (3) (purple) for each GCM during the initial weakening phase (see Table 1) relative to years 1–10. The red and blue bars represent the thermal and haline contributions to $\Delta(\rho_n - \rho_b)$. (b) Bar plot showing the thermal and haline contributions to $\Delta\rho_n$ during the initial weakening phase relative to years 1–10. (c) Bar plot showing the thermal and haline contributions to $\Delta\rho_b$ during the initial weakening phase relative to years 1–10.

During the partial recovery phase, density throughout the Atlantic basin continues to get lighter, as compared to the weakened state. The terms $\Delta\rho_n$ and $\Delta\rho_b$ are more negative than in the weakening phase, but the haline contribution to the density changes is now of comparable size and acts to modulate the response across the different GCMs (Fig. 6). The partial AMOC recovery is associated with a simultaneous warming of the Atlantic basin relative to the high latitudes (cf. red dashed and red dotted lines) and a positive salinity anomaly in the North Atlantic (Figs. 6b,c). During the AMOC weakening, a positive salinity anomaly develops in the subtropical Atlantic basin and can be attributed mainly to the drying of the subtropics, or the “rich-get-richer” mechanism (Durack et al. 2012). After the AMOC weakening, the salinity anomaly moves poleward (not shown) into the North Atlantic between 250 and 1000 m. This northward salinity

transport causes ρ_n to become denser, while the warming at lower latitudes cause ρ_b to become lighter. Together, these processes increase the magnitude of $\rho_n - \rho_b$ and cause $\Delta(\rho_n - \rho_b)$ to become less negative relative to the weakened state (Figs. 6b,c). In CNRM-CM6.1, which undergoes the slowest AMOC recovery, warming occurs throughout the Atlantic basin. However, instead of a positive salinity anomaly in the high latitudes, the haline contribution indicates a freshening, or $\Delta\rho_n < 0$ (blue bar, Fig. 6b). The high-latitude freshening further decreases the meridional density difference and suppresses the AMOC recovery in this GCM.

The primary difference between CNRM-CM6.1, which undergoes the slowest AMOC recovery, and the other GCMs is the high-latitude freshwater anomaly. During the first 100 to 150 years there is a freshening of the high-latitude Atlantic basin in CNRM-CM6.1 (Fig. 7), which could be due to

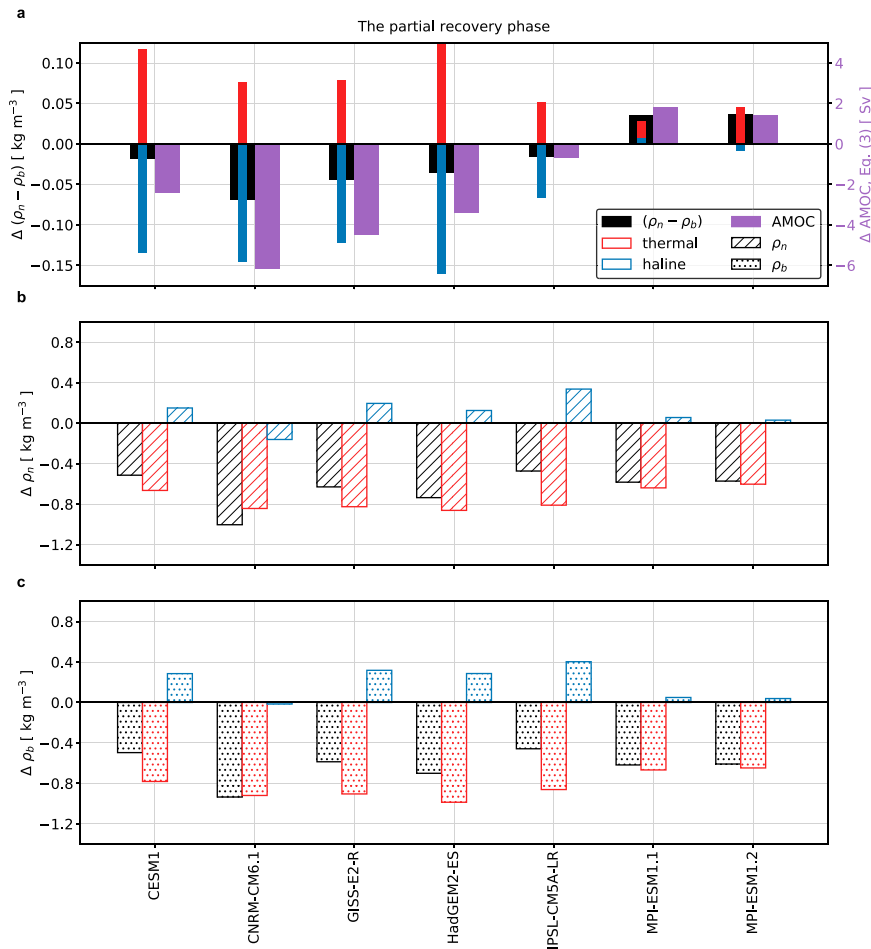


FIG. 6. (a) Bar plot showing the average density change between 250 and 2000 m for $(\rho_n - \rho_b)$ (black) and the maximal change in the meridional overturning circulation streamfunction using Eq. (3) (purple) for each GCM during the partial recovery phase (years 470–500) relative to years 1–10. The red and blue bars represent the thermal and haline contributions to $\Delta(\rho_n - \rho_b)$. (b) Bar plot showing the thermal and haline contributions to $\Delta\rho_n$ during the partial recovery phase relative to years 1–10. (c) Bar plot showing the thermal and haline contributions to $\Delta\rho_b$ during the partial recovery phase relative to years 1–10.

reduced salinity transport by the AMOC weakening, increased sea ice melt, or an intensified hydrological cycle. There is also a convergence of salinity in the subtropical Atlantic basin (30°S–30°N) that is nearly universal across GCMs, although it is weaker in CNRM-CM6.1 (Fig. 7). After 100 to 150 years the subtropical salinity anomaly is transported northward from the subtropical gyre region to the subpolar gyre region and mixes with the fresh high-latitude waters. This salinity anomaly increases the density of the high-latitude subsurface waters and helps to erode the high-latitude vertical stratification, which enables a reinvigoration of convection. In CNRM-CM6.1, which shows little to no AMOC recovery, the local freshening signal overwhelms the salinity anomaly coming from the subtropics (Fig. 7b). Similarly, HadGEM2-ES, which also shows a slower AMOC recovery when compared to other GCMs, experiences larger high-latitude freshening when compared to other GCMs (Fig. 7d).

The two GCMs with the weakest AMOC recovery experience greater Arctic sea ice loss when compared to other GCMs (Fig. 7). In fact, the intermodel spread of trends in AMOC strength between years 470 and 970 is strongly correlated with the percent of remaining Arctic sea ice area during this period (Fig. 8). GCMs with less Arctic sea ice loss tend to show stronger AMOC recoveries, whereas GCMs with more Arctic sea ice loss tend to show weaker AMOC recoveries (Fig. 8). At the end of the simulation in CNRM-CM6.1, the AMOC has a slight positive trend and the freshening signal begins to erode (Fig. 7b), suggesting that during a longer simulation a recovery may ultimately occur after a sufficiently large buildup of salinity at the low latitudes. Another possible explanation for the large freshening of the subpolar gyre region is the AMOC weakening itself, which can reduce salinity transport to the North Atlantic. However, there is no significant relationship between the magnitude of AMOC

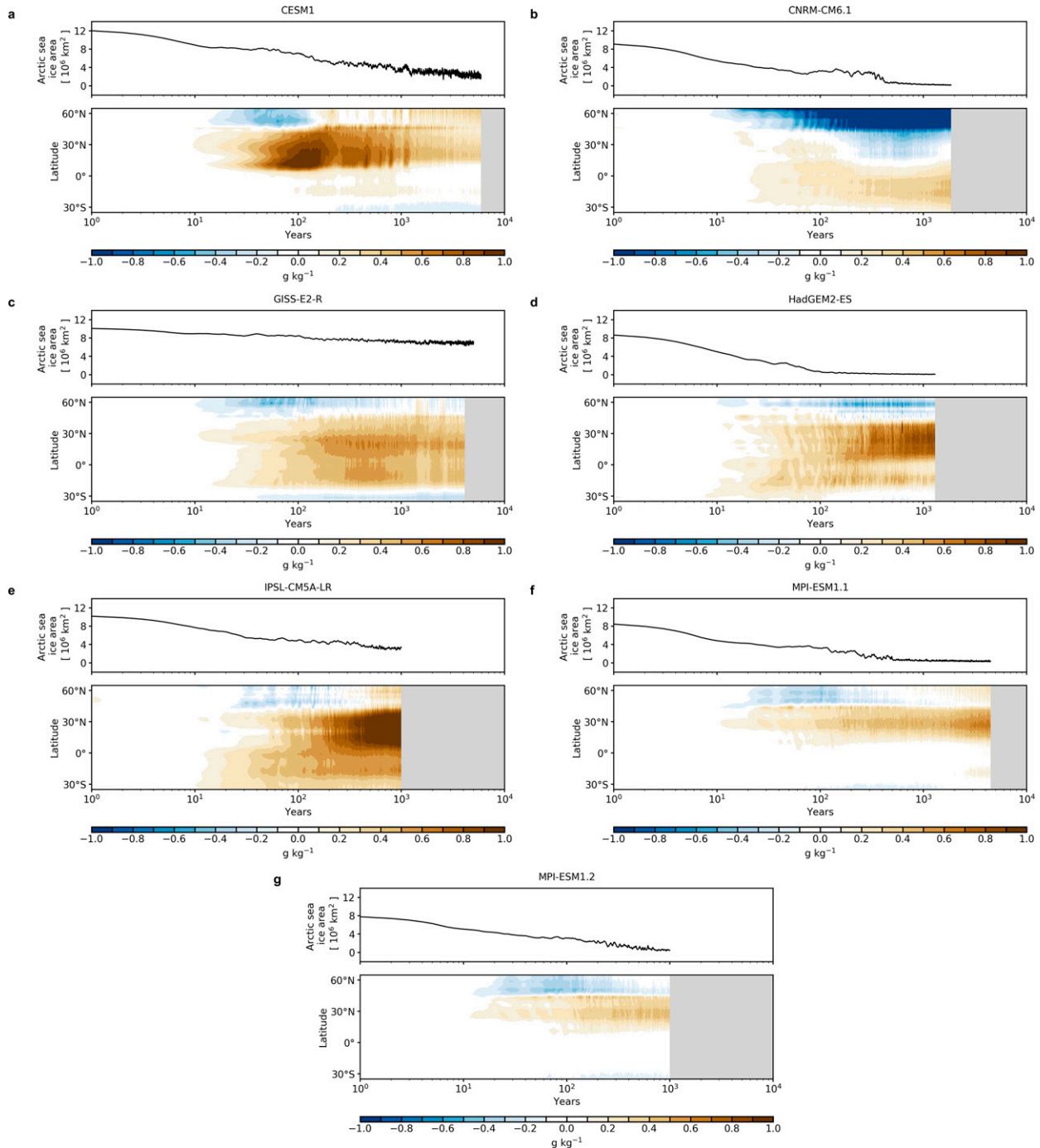


FIG. 7. Hovmöller plot of the anomalous zonally averaged salinity in the Atlantic basin, vertically averaged between 250 and 2000 m, for (a) CESM1, (b) CNRM-CM6.1, (c) GISS-E2-R, (d) HadGEM2-ES, (e) IPSL-CM5A-LR, (f) MPI-ESM1.1, and (g) MPI-ESM1.2. A Savitzky–Golay filter with a window size of 11 years was applied to all time series. All anomalies are calculated relative to an average of years 1–10. The upper plot in each panel shows annual Arctic sea ice area for each GCM.

weakening and freshening of the subpolar gyre region across the various GCMs, indicating that other sources of freshening are at play. Note that CNRM-CM6.1 warms more than other GCMs, suggesting that changes to precipitation minus evaporation ($P - E$) may be larger in the high latitudes in this GCM, following

the “wet-gets-wetter, dry-gets-drier” paradigm (Held and Soden 2006). This means that there would also be greater $P - E$ input into the ocean, and suggests that while sea ice loss alone is not responsible for all of the freshening, it could play a role in initiating greater freshwater input into the high-latitude North Atlantic.

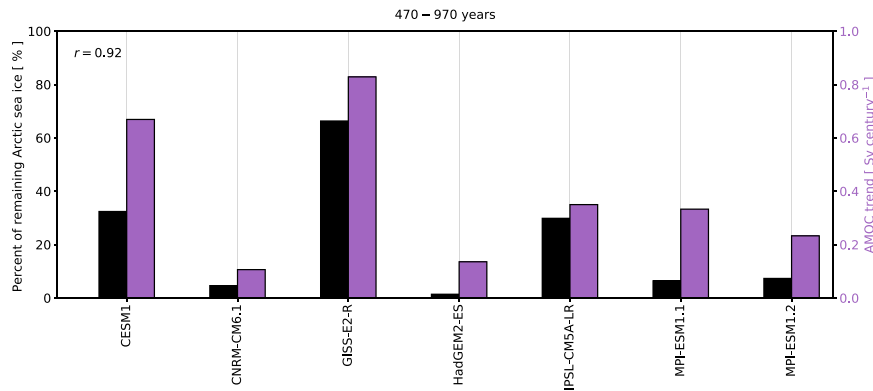


FIG. 8. Bar plot showing the percentage of remaining Arctic sea ice relative to the initial state (years 1–10) (black) and the corresponding AMOC trend for years 470–970 (purple) in each GCM. The Pearson correlation coefficient between the two is shown in the upper-left-hand corner.

c. The restrengthening phase and equilibrium response

During the restrengthening phase of the AMOC (years 970–1000), $\Delta(\rho_n - \rho_b) > 0$ for more than half of the GCMs (Fig. 9a). That is, the meridional density difference becomes stronger when compared to the initial state. However, for CNRM-CM6.1 and HadGEM2-ES, which both experience a prolonged AMOC weakening and weak recovery, $\Delta(\rho_n - \rho_b)$ remains negative. Note that $\Delta(\rho_n - \rho_b)$ also remains negative for GISS-E2-R, but it is less negative when compared to the partial recovery phase. In the GCMs that show positive values of $\Delta(\rho_n - \rho_b)$ during the restrengthening phase, the implied overturning from the TWR is approximately 2–6 Sv stronger than the initial strength (Fig. 9a). For MPI-ESM1.1 and MPI-ESM1.2, the overturning is also deeper than the initial state (not shown).

A decomposition of the thermal and haline contributions to $\Delta\rho_n$ and $\Delta\rho_b$ shows that the positive values of $\Delta(\rho_n - \rho_b)$ are driven mainly by warming throughout the Atlantic basin (Figs. 9a–c). In contrast to the weakening phase, here $\Delta\rho_b$ becomes less dense due to more warming (Figs. 9b,c), and $|\Delta\rho_b|$ is now greater than $|\Delta\rho_n|$, strengthening the meridional density difference. The increase in the basinwide density contrast supports an overturning that is stronger than the initial state. For most GCMs salinity acts to reduce the basinwide density contrast. GCMs with a slow AMOC recovery (CNRM-CM6.1 and HadGEM2-ES) have larger negative values of $\Delta(\rho_n - \rho_b)$, largely due to the haline component.

For all of the GCMs that simulate multiple millennia, $\Delta(\rho_n - \rho_b) > 0$, meaning that $\rho_n - \rho_b$ exceeds its initial state and supports a stronger overturning than the initial state (Fig. 10a). During the equilibrium phase, the increase in $\rho_n - \rho_b$ is primarily due to warming of the low-latitude Atlantic basin, which contributes a 0.05–0.10 kg m^{-3} increase in the meridional density difference. The salinity anomaly becomes weaker for $\Delta\rho_b$ and $\Delta\rho_n$, but modulates the magnitude of the basinwide density difference (Figs. 10b,c). Previous studies have attributed this low-latitude warming in

the Atlantic basin to reduced upwelling in the tropical region (e.g., Stouffer and Manabe 2003). Another possible explanation for the long time scale low-latitude warming is a deepening of isopycnals that is related to the initial AMOC weakening (Sun et al. 2020b, 2022). Additionally, changes in the Southern Ocean surface buoyancy flux could impact warming at middepth in the Atlantic basin (Jansen and Nadeau 2016) and be related to Southern Ocean heat uptake and subduction in Antarctic Intermediate Water density classes.

5. Discussion

a. Surface-forced water mass transformation

Across all of the GCMs, the interior density distribution and its evolution in response to $4 \times \text{CO}_2$ provides a framework for understanding transitions in the strength and structure of the AMOC. Ultimately, however, changes in meridional overturning must be closed by surface and interior rates of water mass transformation between density classes. An alternative approach to understanding controls on the strength of the AMOC acknowledges that the overturning delivers waters to regions of water mass transformation (Newsom and Thompson 2018) and its structure in density space can be inferred from the surface-forced water mass transformation (e.g., Walin 1982; Speer and Tziperman 1992; Groeskamp et al. 2019).

Surface-forced water mass transformation quantifies the circulation between density classes sustained by surface buoyancy fluxes from heat and freshwater forcing components. To illustrate the connection between surface and interior circulation changes, we calculate the surface-forced water mass transformation for two GCMs (CESM1 and CNRM-CM6.1) that provide the output needed to diagnose these processes. While this analysis cannot be performed on all GCMs due to a most GCMs missing various surface fluxes, CESM1 and CNRM-CM6.1 fortunately represent the end members of the strong and weak AMOC recoveries.

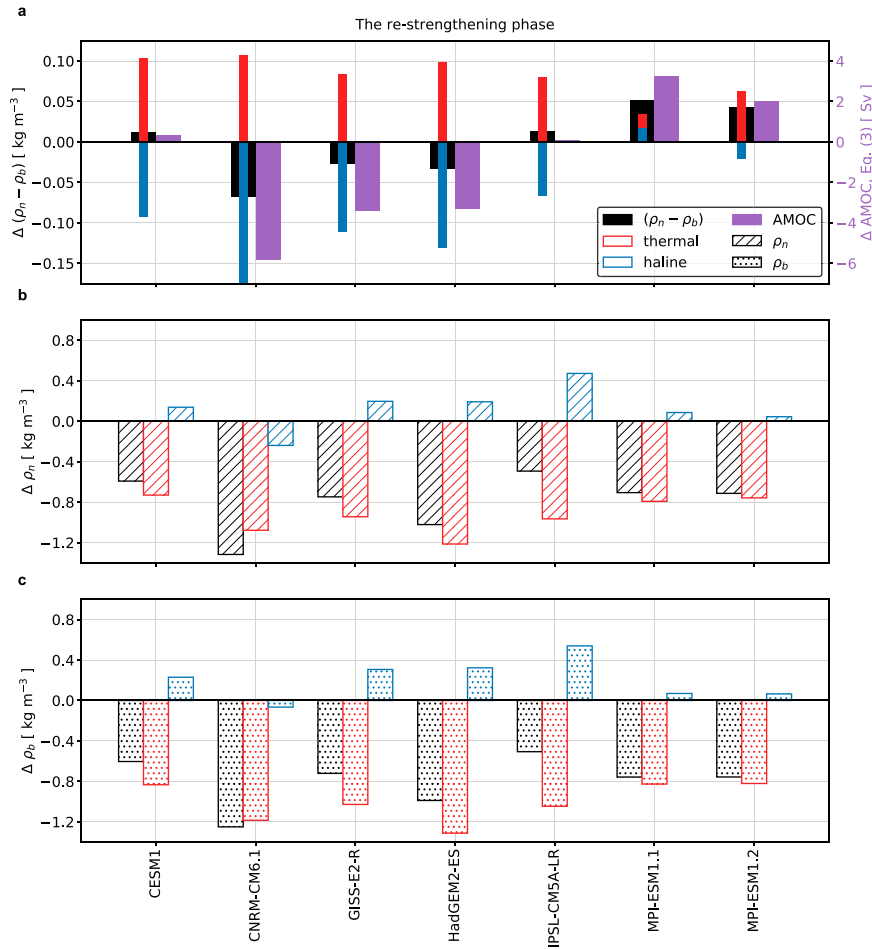


FIG. 9. (a) Bar plot showing the average density change between 250 and 2000 m for $(\rho_n - \rho_b)$ (black) and the maximal change in the meridional overturning circulation streamfunction using Eq. (3) (purple) for each GCM during the restrengthening phase (years 970–1000) relative to years 1–10. The red and blue bars represent the thermal and haline contributions to $\Delta(\rho_n - \rho_b)$. (b) Bar plot showing the thermal and haline contributions to $\Delta\rho_n$ during the restrengthening phase relative to years 1–10. (c) Bar plot showing the thermal and haline contributions to $\Delta\rho_b$ during the restrengthening phase relative to years 1–10.

Following Walin (1982), the circulation across a given density class can be quantified as

$$F(y, \sigma) = \frac{\partial}{\partial \sigma} \int_{A[\sigma' > \sigma]} D(x, y, t) \mathcal{H}[\sigma'(x) - \sigma_{\min}(y)] dA, \quad (4)$$

where

$$D(x, y, t) = -\frac{\alpha(x, y, t)}{c_p} Q_H(x, y, t) + \beta(x, y, t) S(x, y, t) Q_F(x, y, t) \quad (5)$$

is the surface density flux, α and β are the thermal expansion and haline contraction coefficients, Q_H and Q_F are the surface heat and freshwater fluxes (kg m⁻² s⁻¹), respectively, S is the surface absolute salinity, and c_p is the specific heat capacity of

seawater (4186 J kg⁻¹ K⁻¹). Here, the surface heat and freshwater fluxes are defined to be positive into the ocean. The term F has units of m³ s⁻¹ and represents the formation of water masses as a function of density. In Eq. (4), $\sigma_{\min}(y)$ is the minimum density at latitude y , and A is the surface outcrop area for all densities greater than a given density σ . Equation (4) can be decomposed into contributions to the buoyancy flux from heat and freshwater.

Applying Eq. (4) to CESM1 and CNRM-CM6.1 indicates that the formation of NADW is largely heat-driven and that changes to the formation rate of NADW are also largely heat-driven (Fig. 11). During the initial state, CESM1 and CNRM-CM6.1 both have two peaks of transformation rates around $\sigma_0 = 1024$ and 1027 kg m⁻³. Approximately 1000 years after the $4 \times \text{CO}_2$ forcing, surface-forced water mass transformation occurs in lighter density classes for each GCM,

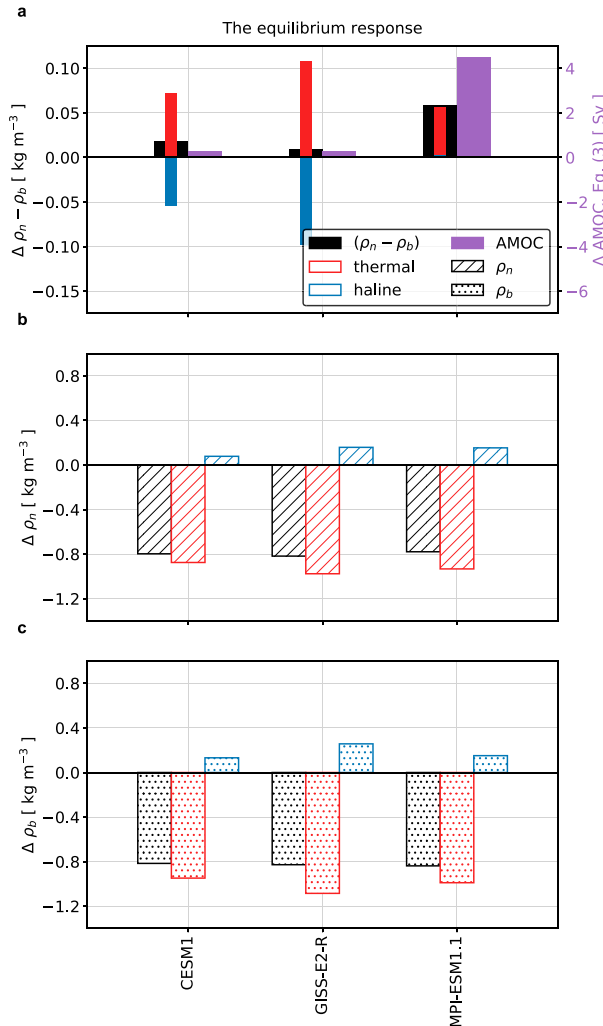


FIG. 10. (a) Bar plot showing (black) the average density change between 250 and 2000 m for $(\rho_n - \rho_b)$ and (purple) the maximal change in the meridional overturning circulation streamfunction using Eq. (3) for each GCM during the equilibrium response (years 3500–3530) relative to years 1–10. The red and blue bars represent the thermal and haline contributions to $\Delta(\rho_n - \rho_b)$. (b) Bar plot showing the thermal and haline contributions to $\Delta\rho_n$ during the equilibrium response relative to years 1–10. (c) Bar plot showing the thermal and haline contributions to $\Delta\rho_b$ during the equilibrium response relative to years 1–10.

primarily because the ocean warms. During the restrengthening phase (years 970–1000), when CESM1 shows a recovered AMOC and CNRM-CM6.1 shows a weakened AMOC, the peak transformation rate around 1027 kg m^{-3} is notably absent in CNRM-CM6.1. To understand causes of these changes, we compute the surface-forced water mass transformation using either the initial density field and the surface flux field from years 970–1000 or the initial surface flux field and the density field from years 970–1000. This enables us to identify mechanisms of NADW changes. A decomposition of these changes due to either changes in the surface density field (dotted line) and the surface fluxes

(dash-dotted) shows that this decrease in the transformation rate is largely the result of changes in the surface density field. In CNRM-CM6.1, the sustained freshening limits the ability of convection associated with heat loss to penetrate deep into the water column. However, in CESM1 changes to the density field are much smaller, enabling the heat loss to penetrate to greater depth.

The LongRunMIP repository lacks sufficient output to apply Eq. (4) to all GCMs. Still, the surface-forced water mass transformation changes (Fig. 11) support the idea of large freshwater anomalies in the surface ocean inhibiting deep convection, which prevents an AMOC recovery. The freshwater anomalies stratify the surface density field and effectively cut off the interior isopycnals from reaching the surface. These transformation rates show that the competition between a high-latitude freshwater anomaly and low-latitude salinity anomaly can determine the timing and magnitude of an AMOC recovery. Further work, however, is required to understand how the formation of surface waters interacts with local and nonlocal processes to suppress deep-water formation.

b. Mechanisms for a partial recovery of the Atlantic overturning circulation

Our results indicate that the recovery of the AMOC is associated with two simultaneous processes: 1) a warming of the Atlantic basin relative to the North Atlantic and 2) a subtropical salinity anomaly that moves poleward. The former enhances the Atlantic meridional density difference, while the latter erodes the near-surface stratification and reinvigorates deep convection. Figure 12 shows a schematic of the processes that contribute to the time evolution of the AMOC in response to $4 \times \text{CO}_2$ in coupled GCMs. During the initial weakening, all GCMs show a warming of the North Atlantic water column, although some GCMs warm more (and the AMOC weakens more) than others. After the initial weakening, GCMs with a strong AMOC recovery (e.g., CESM1) have positive salinity anomaly in the North Atlantic, whereas GCMs with a weak AMOC recovery (e.g., CNRM-CM6.1 and HadGEM2-ES) have either a weak positive salinity anomaly or a negative anomaly indicative of high-latitude freshening (Fig. 12). All GCMs show greater warming of the Atlantic basin relative to the North Atlantic during the recovery phase, but the degree of high-latitude freshening correlates strongly with the level of the AMOC recovery. This highlights the role that high-latitude freshwater changes play in generating differences in the magnitude and rate of AMOC recovery across GCMs in response to the same external forcing.

Our results are both similar to and different from other studies that have examined the transient and equilibrium responses of the AMOC to surface warming by considering the relative role of thermal and haline contributions to circulation changes. For instance, the recovery of the AMOC in ocean-only models is attributed to a density reduction in the lower thermocline of the high latitudes (Jansen et al. 2018; Jansen and Nadeau 2019), but it is unclear whether this modification results from temperature or salinity changes as these models only simulate buoyancy. Other studies, which use coupled

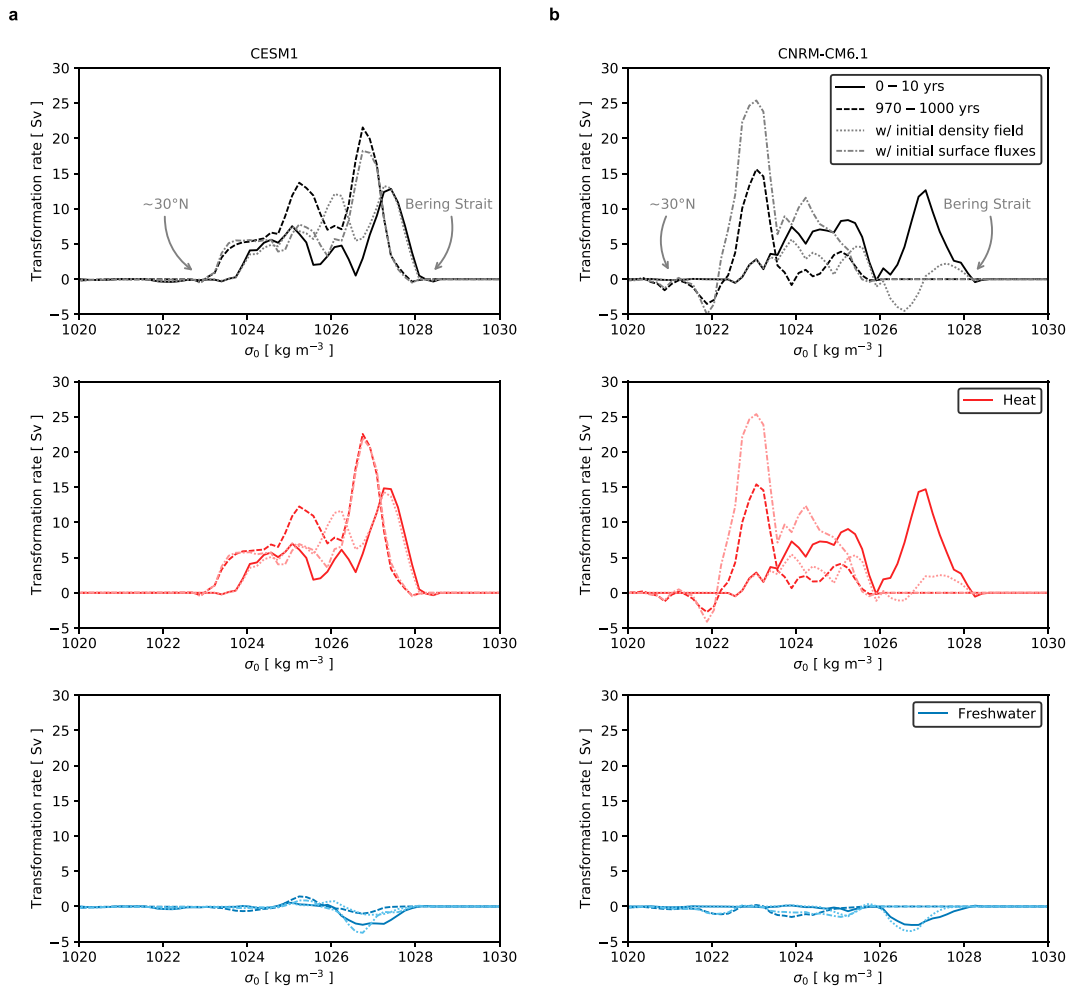


FIG. 11. Surface-forced water mass transformation, Eq. (4), in the North Atlantic (north of 30°N) in (a) CESM1 and (b) CNRM-CM6.1. CESM1 simulates a strong AMOC recovery whereas the AMOC in CNRM-CM6.1 essentially has no recovery over the period simulated. Surface transformation is calculated as a function of potential density referenced to the surface (σ_0). (top) The total transformation from all diabatic processes is provided in black, which sums contributions from (middle) heat and (bottom) freshwater. The solid lines indicates the initial state (years 1–10) and the dashed line indicates the years 970–1000. The light-colored lines denote the transformation rates for the years 970–1000 but with either the initial density field (dotted) or initial surface flux field (dash-dotted). For visualization, approximate geographical boundaries are labeled. Here, positive transformation represents a volume flux toward denser classes.

GCMs, have found that the AMOC recovery is associated with salinity anomalies that reduce high-latitude stratification and reinvigorate convection (Vellinga et al. 2002; Yin and Stouffer 2007; Krebs and Timmermann 2007; Wu et al. 2011; Sigmond et al. 2020; Zhu and Liu 2020; Ackermann et al. 2020). While we indeed find that salinity anomalies play an important role in the AMOC recovery, the role of salinity is more nuanced than previously suggested. Our results indicate that the interplay of temperature changes, which warm the Atlantic basin, and salinity anomalies, which densify the high-latitude ocean, set the magnitude of the AMOC recovery. This stands in contrast to Wu et al. (2011) and Sigmond et al. (2020), who argue that salinity is the primary driver of the AMOC recovery. In this study, we focus on the rate and

magnitude of the AMOC recovery, whereas other studies have looked at the role of salinity in setting the stability of the AMOC. Indeed, the poleward movement of salinity and magnitude of high-latitude freshening might itself be related to the AMOC stability indicator, which relates the AMOC recovery to net freshwater input into the Atlantic basin (Liu et al. 2014, 2017; Li et al. 2021). The advection of salinity from the low latitudes, which competes with the high-latitude freshening in the North Atlantic, might help explain the intermodel variability in AMOC recovery. Future work should explore how the mechanistic explanation of this study, which details the origins of these freshwater and salinity anomalies, relates to the AMOC stability metric of these other studies (e.g., Liu et al. 2014, 2017). Previous studies have shown that

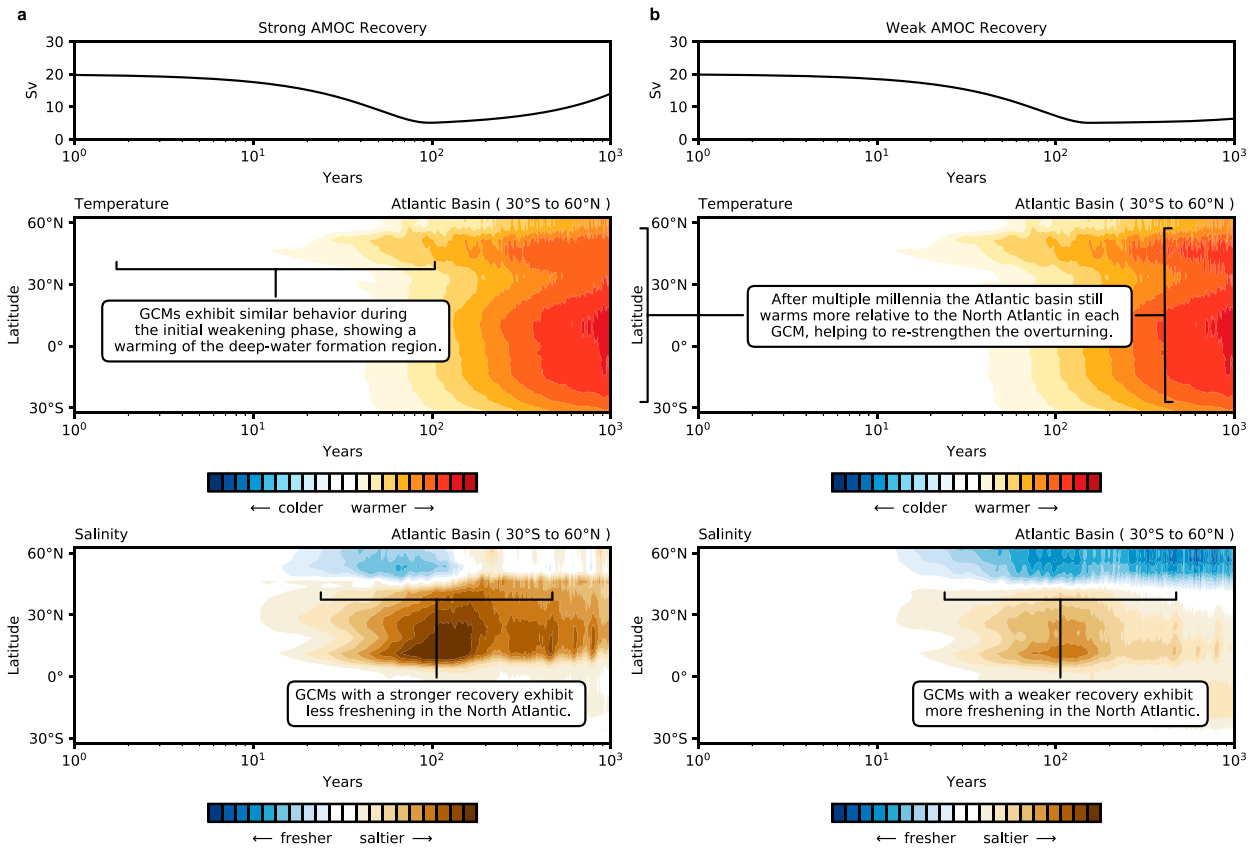


FIG. 12. Schematic depicting a GCM with a (a) strong AMOC recovery and (b) weak AMOC recovery or a prolonged weakening AMOC phase. (middle) Temperature changes in the Atlantic basin and (bottom) salinity changes in the Atlantic basin. There are three phases: a weakening phase, which is characterized by a warming of the high-latitude North Atlantic; a partial recovery phase or prolonged weakening phase, which is characterized by a warming of the Atlantic basin and an increase or decrease in salinity of the high-latitude North Atlantic; and a restrengthening phase, which is characterized by a warming of the low-latitude Atlantic basin. Warming of the low-latitude Atlantic basin is similar across all GCMs. The major feature that distinguishes GCMs with faster and slower AMOC recoveries is the salinity anomalies in the high-latitude North Atlantic. A subtropical salinity anomaly forms when the AMOC is weakened and then is advected to the high latitudes by the subtropical gyre. GCMs with slower AMOC recoveries instead show a freshening of the high-latitude North Atlantic, which is linked to large differences in sea ice melt across the GCMs. This suggests that the representation of sea ice and other high-latitude freshwater sources in coupled GCMs is critical for representing the future evolution of the AMOC.

the AMOC response can be sensitive to the [Zhu et al. \(2014, 2015\)](#) forcing or a different radiative forcing ([Rugenstein et al. 2016b](#)). For example, it has been shown that the AMOC does not weaken as much with increasing carbon dioxide when starting from Last Glacial Maximum climate conditions ([Zhu et al. 2015](#)), and possibly exhibits a two-stage recovery ([Zhu et al. 2014](#)). Understanding how robust the results of this paper are for various climate states is important for understanding past AMOC transitions.

The equilibrium response of the AMOC in ocean-only models has been attributed to a diffusive adjustment of abyssal density, in response to a modification in bottom waters exported from the Southern Ocean ([Jansen et al. 2018](#)). Given that the LongRunMIP simulations are at most 5900 years long, and some have still not reached a new steady state, it is difficult to attribute the equilibrium response to precise mechanisms, such as localized basin dynamics, interbasin transport, or Southern Ocean processes. While the restrengthening

phase of the AMOC is linked to low-latitude Atlantic warming based on the TWR, this does not necessarily imply that the AMOC evolution results from processes occurring in the Atlantic basin alone. Recently, [Newsom and Thompson \(2018\)](#) and [Holmes et al. \(2019\)](#) have revisited the ocean's buoyancy and heat budget, respectively, and found that much of the heat loss in the North Atlantic is balanced by heat uptake in the low-latitude Indo-Pacific, rather than the low-latitude Atlantic. This zonal imbalance is enabled by the much larger areal extent of the low-latitude Indo-Pacific, and the transfer of heat to the Atlantic through the upper ocean's interbasin overturning circulation ([Gordon 1986](#); [Newsom et al. 2021](#)). The dynamics of interbasin exchange, mediated by both the Southern Ocean and low-latitude pathways such as the Indonesian Throughflow and the Aghulas Retroflexion, over millennial time scales remains largely unstudied. Additionally, changes in Southern Ocean water mass transformation could modify the vertical stratification of the Atlantic

basin and play a role in determining the AMOC (Jansen and Nadeau 2016; Sun et al. 2018). It has been shown that long-term equilibration of the deep ocean is sensitive to the properties of Antarctic Bottom Water (AABW), which evolves on multi-millennial time scales. The representation of AABW formation in the LongRunMIP is a potential source of uncertainty that is not explored in this present study (Heuzé et al. 2015).

c. Utility and limitations of LongRunMIP

The LongRunMIP simulations provide the first model intercomparison of the long-term evolution of the AMOC in response to abrupt forcing. Even so, the longest simulation in this study is 5900 years. Recent work has shown that the AMOC continues to change, following warming, on time scales out to 10 000–15 000 years (Rugenstein et al. 2016b; Jansen et al. 2018; Jansen and Nadeau 2019). Thus, even the LongRunMIP simulations are too short to capture all of the processes that influence the AMOC evolution, especially long-term mechanisms such as the diffusive adjustment of the deep ocean (Jansen et al. 2018).

Because LongRunMIP is a MIP of opportunity, without an agreed-upon protocol, model output is not uniformly reported, making it hard to precisely attribute the intermodel spread in the AMOC recovery to a specific process. For instance, it would be helpful to have ocean velocity fields as the relative role of changes in surface forcing versus changes in salinity and temperature due to ocean circulation changes could be quantified (e.g., Garuba and Rasch 2020). Similarly, the lack of uniform output makes it difficult to partition freshwater changes into $P - E$, runoff, and ice fluxes. Indeed, GCMs with a slower AMOC recovery tend to have greater Arctic sea ice loss and high-latitude freshwater input, which likely limits the ability of the subtropical salinity anomaly to reduce high-latitude stratification and reinvigorate convection. However, additional work is required to assess the gradual recovery of the AMOC and the role of Arctic sea ice loss, or other freshwater sources such as changes to the hydrologic cycle or ice sheet processes. CNRM-CM6.1, for instance, which experiences a prolonged AMOC weakening, tends to warm much more than other GCMs (Rugenstein et al. 2019), which corresponds to $P - E$ being larger in the high latitudes following the “wet gets wetter, dry gets drier” paradigm (Held and Soden 2006). Thus, the correlation between Arctic sea ice loss and AMOC strength (Fig. 8) may arise from an indirect mechanism related to the amplification of the existing pattern of $P - E$ (Pithan and Jung 2021). Inclusion of temperature and salinity in toy models similar to those of Jansen and Nadeau (2019) and Nadeau and Jansen (2020), could be used to explore parameter space that can impact long-term ocean circulation changes. Such work may also permit a better theoretical understanding of how salinity and temperature interact and influence the response of the AMOC to external forcing.

Finally, an important caveat of this work is that the GCMs do not resolve ocean mesoscale eddies or dynamics of narrow, boundary currents in the North Atlantic. In response to warming

and freshwater perturbations, higher-resolution GCMs exhibit markedly different changes to ocean circulation (Mecking et al. 2016; Newsom et al. 2016; Gent 2018; Jackson et al. 2020; Hirschi et al. 2020) and often experience less weakening of the AMOC when compared to low-resolution GCMs (e.g., Li et al. 2021; Jackson et al. 2020). Further investigation of the transient and equilibrium responses of the AMOC to increased greenhouse gas concentrations with high-resolution eddy-resolving GCMs may modify the relative importance of haline and thermal contributions to AMOC changes at different time scales. For example, higher-resolution ocean models have been shown to change the magnitude of the subtropical gyre transport (e.g., Lévy et al. 2010), which could impact the northward advection of salinity that erodes near-surface stratification and reinvigorate deep convection.

6. Conclusions

This study examines the transient and equilibrium responses of the AMOC to warming in an unprecedented collection of millennial-length climate simulations from atmosphere–ocean GCMs. We introduce a framework for understanding the various AMOC responses in each GCM using a simple thermal wind expression, which relates the overturning circulation in the North Atlantic to the density difference between the region of deep-water formation and the Atlantic basin. We find that this expression captures the initial weakening of the AMOC on centennial time scales and various levels of AMOC recoveries as simulated by GCMs in response to $4 \times \text{CO}_2$ forcing.

Using the thermal wind expression, we attribute the evolution of the AMOC on different time scales to changes in temperature and salinity in distinct regions. The universal weakening of the AMOC across GCMs is dominated by warming of the northern convection region. The partial recovery of the AMOC, which occurs in most GCMs, results from both a simultaneous warming of the Atlantic basin and an increase in salinity in the North Atlantic. The positive salinity anomaly forms in the subtropical Atlantic first when the AMOC is weakened, and is then advected northward, which erodes the stratification of the North Atlantic and reinvigorates deep convection. The timing and magnitude of the AMOC recovery, at least in the LongRunMIP simulations, is related to the amount of freshwater input in the North Atlantic: GCMs with a slower AMOC recovery tend to show increased Arctic sea ice loss compared to GCMs with a faster AMOC recovery. This suggests it will be crucial to monitor Arctic sea ice loss and other high-latitude freshwater sources throughout and beyond the twenty-first century, as it may ultimately determine whether the AMOC will recover. Finally, the eventual strengthening of the AMOC, which takes multiple millennia, is linked to low-latitude warming of the Atlantic basin. For the simulations that span multiple millennia, the AMOC becomes stronger than the initial state despite having vastly different distributions of temperature and salinity. This work provides a framework for assessing the relative importance of temperature and salinity dynamics in the evolution of the AMOC. A similar approach may help identify whether the

AMOC is likely to experience a fast or slow recovery beyond the twenty-first century, or if the AMOC has experienced a slow recovery during past climate changes.

Acknowledgments. The research would not have been possible without the efforts of the contributors to the Long-RunMIP project, which is freely available at <http://www.longrunmip.org/>. The authors thank Sarah Ragen for helpful comments on an earlier version of this paper. D.B.B. was supported by an American Meteorological Society (AMS) Graduate Fellowship and the National Science Foundation Graduate Research Fellowship Program (NSF Grant DGE-1745301). A.F.T. and S.S. were supported by NSF Grant OCE-1756956 and OCE-2023259. E.R.N. was supported by NERC Project NE/P019218/1 on transient tracer-based Investigation of Circulation and Thermal Ocean Change (TICTOC).

Data availability statement. The code for this study is available at <https://github.com/dbonan/bonan-et-al-2022-Journal-of-Climate>. The data for this study are freely available at <http://www.longrunmip.org/>.

REFERENCES

- Ackermann, L., C. Danek, P. Gierz, and G. Lohmann, 2020: AMOC recovery in a multicentennial scenario using a coupled atmosphere–ocean–ice sheet model. *Geophys. Res. Lett.*, **47**, e2019GL086810, <https://doi.org/10.1029/2019GL086810>.
- Andrews, T., J. M. Gregory, and M. J. Webb, 2015: The dependence of radiative forcing and feedback on evolving patterns of surface temperature change in climate models. *J. Climate*, **28**, 1630–1648, <https://doi.org/10.1175/JCLI-D-14-00545.1>.
- Bakker, P., and Coauthors, 2016: Fate of the Atlantic meridional overturning circulation: Strong decline under continued warming and Greenland melting. *Geophys. Res. Lett.*, **43**, 12 252–12 260, <https://doi.org/10.1002/2016GL070457>.
- Broecker, W. S., 1997: Thermohaline circulation, the Achilles heel of our climate system: Will man-made CO₂ upset the current balance? *Science*, **278**, 1582–1588, <https://doi.org/10.1126/science.278.5343.1582>.
- , 1998: Paleoocean circulation during the last deglaciation: A bipolar seesaw? *Paleoceanography*, **13**, 119–121, <https://doi.org/10.1029/97PA03707>.
- , 2003: Does the trigger for abrupt climate change reside in the ocean or in the atmosphere? *Science*, **300**, 1519–1522, <https://doi.org/10.1126/science.1083797>.
- Buckley, M. W., and J. Marshall, 2016: Observations, inferences, and mechanisms of the Atlantic meridional overturning circulation: A review. *Rev. Geophys.*, **54**, 5–63, <https://doi.org/10.1002/2015RG000493>.
- Burke, A., A. L. Stewart, J. F. Adkins, R. Ferrari, M. F. Jansen, and A. F. Thompson, 2015: The glacial mid-depth radiocarbon bulge and its implications for the overturning circulation. *Paleoceanography*, **30**, 1021–1039, <https://doi.org/10.1002/2015PA002778>.
- Butler, E., K. Oliver, J.-M. Hirschi, and J. Mecking, 2016: Reconstructing global overturning from meridional density gradients. *Climate Dyn.*, **46**, 2593–2610, <https://doi.org/10.1007/s00382-015-2719-6>.
- Cheng, W., J. C. Chiang, and D. Zhang, 2013: Atlantic meridional overturning circulation (AMOC) in CMIP5 models: RCP and historical simulations. *J. Climate*, **26**, 7187–7197, <https://doi.org/10.1175/JCLI-D-12-00496.1>.
- Curry, W. B., and D. W. Oppo, 2005: Glacial water mass geometry and the distribution of $\delta^{13}\text{C}$ of ΣCO_2 in the western Atlantic Ocean. *Paleoceanography*, **20**, PA1017, <https://doi.org/10.1029/2004PA001021>.
- de Boer, A. M., A. Gnanadesikan, N. R. Edwards, and A. J. Watson, 2010: Meridional density gradients do not control the Atlantic overturning circulation. *J. Phys. Oceanogr.*, **40**, 368–380, <https://doi.org/10.1175/2009JPO4200.1>.
- Dixon, K. W., T. L. Delworth, M. J. Spelman, and R. J. Stouffer, 1999: The influence of transient surface fluxes on North Atlantic overturning in a coupled GCM climate change experiment. *Geophys. Res. Lett.*, **26**, 2749–2752, <https://doi.org/10.1029/1999GL900571>.
- Dufresne, J.-L., and Coauthors, 2013: Climate change projections using the IPSL-CM5 Earth system model: From CMIP3 to CMIP5. *Climate Dyn.*, **40**, 2123–2165, <https://doi.org/10.1007/s00382-012-1636-1>.
- Durack, P. J., S. E. Wijffels, and R. J. Matear, 2012: Ocean salinities reveal strong global water cycle intensification during 1950 to 2000. *Science*, **336**, 455–458, <https://doi.org/10.1126/science.1212222>.
- Ferrari, R., M. F. Jansen, J. F. Adkins, A. Burke, A. L. Stewart, and A. F. Thompson, 2014: Antarctic sea ice control on ocean circulation in present and glacial climates. *Proc. Natl. Acad. Sci. USA*, **111**, 8753–8758, <https://doi.org/10.1073/pnas.1323922111>.
- Frierson, D. M., and Coauthors, 2013: Contribution of ocean overturning circulation to tropical rainfall peak in the Northern Hemisphere. *Nat. Geosci.*, **6**, 940–944, <https://doi.org/10.1038/ngeo1987>.
- Frölicher, T., M. Aschwanen, N. Gruber, S. Jaccard, J. Dunne, and D. Paynter, 2020: Contrasting upper and deep ocean oxygen response to protracted global warming. *Global Biogeochem. Cycles*, **34**, e2020GB006601, <https://doi.org/10.1029/2020GB006601>.
- Ganachaud, A., and C. Wunsch, 2003: Large-scale ocean heat and freshwater transports during the World Ocean Circulation Experiment. *J. Climate*, **16**, 696–705, [https://doi.org/10.1175/1520-0442\(2003\)016<0696:L.SOHAF>2.0.CO;2](https://doi.org/10.1175/1520-0442(2003)016<0696:L.SOHAF>2.0.CO;2).
- Garuba, O. A., and P. J. Rasch, 2020: A partial coupling method to isolate the roles of the atmosphere and ocean in coupled climate simulations. *J. Adv. Model. Earth Syst.*, **12**, e2019MS002016, <https://doi.org/10.1029/2019MS002016>.
- Gebbie, G., 2014: How much did glacial North Atlantic water shoal? *Paleoceanography*, **29**, 190–209, <https://doi.org/10.1002/2013PA002557>.
- Gent, P. R., 2018: A commentary on the Atlantic meridional overturning circulation stability in climate models. *Ocean Modell.*, **122**, 57–66, <https://doi.org/10.1016/j.ocemod.2017.12.006>.
- Gnanadesikan, A., 1999: A simple predictive model for the structure of the oceanic pycnocline. *Science*, **283**, 2077–2079, <https://doi.org/10.1126/science.283.5410.2077>.
- Gordon, A. L., 1986: Interocean exchange of thermocline water. *J. Geophys. Res.*, **91**, 5037–5046, <https://doi.org/10.1029/JC091iC04p05037>.
- Gregory, J., and Coauthors, 2005: A model intercomparison of changes in the Atlantic thermohaline circulation in response to increasing atmospheric CO₂ concentration. *Geophys. Res. Lett.*, **32**, L12703, <https://doi.org/10.1029/2005GL023209>.

- Groeskamp, S., S. M. Griffies, D. Iudicone, R. Marsh, A. G. Nurser, and J. D. Zika, 2019: The water mass transformation framework for ocean physics and biogeochemistry. *Annu. Rev. Mar. Sci.*, **11**, 271–305, <https://doi.org/10.1146/annurev-marine-010318-095421>.
- Haskins, R. K., K. I. Oliver, L. C. Jackson, S. S. Drijfhout, and R. A. Wood, 2019: Explaining asymmetry between weakening and recovery of the AMOC in a coupled climate model. *Climate Dyn.*, **53**, 67–79, <https://doi.org/10.1007/s00382-018-4570-z>.
- , —, —, R. A. Wood, and S. S. Drijfhout, 2020: Temperature domination of AMOC weakening due to freshwater hosing in two GCMs. *Climate Dyn.*, **54**, 273–286, <https://doi.org/10.1007/s00382-019-04998-5>.
- He, C., Z. Liu, and A. Hu, 2019: The transient response of atmospheric and oceanic heat transports to anthropogenic warming. *Nat. Climate Change*, **9**, 222–226, <https://doi.org/10.1038/s41558-018-0387-3>.
- Held, I. M., and B. J. Soden, 2006: Robust responses of the hydrological cycle to global warming. *J. Climate*, **19**, 5686–5699, <https://doi.org/10.1175/JCLI3990.1>.
- Heuzé, C., K. J. Heywood, D. P. Stevens, and J. K. Ridley, 2015: Changes in global ocean bottom properties and volume transports in CMIP5 models under climate change scenarios. *J. Climate*, **28**, 2917–2944, <https://doi.org/10.1175/JCLI-D-14-00381.1>.
- Hirschi, J. J.-M., and Coauthors, 2020: The Atlantic meridional overturning circulation in high-resolution models. *J. Geophys. Res. Oceans*, **125**, e2019JC015522, <https://doi.org/10.1029/2019JC015522>.
- Holmes, R. M., J. D. Zika, R. Ferrari, A. F. Thompson, E. R. Newsom, and M. H. England, 2019: Atlantic Ocean heat transport enabled by Indo-Pacific heat uptake and mixing. *Geophys. Res. Lett.*, **46**, 13 939–13 949, <https://doi.org/10.1029/2019GL085160>.
- Jackson, L. C., 2013: Shutdown and recovery of the AMOC in a coupled global climate model: The role of the advective feedback. *Geophys. Res. Lett.*, **40**, 1182–1188, <https://doi.org/10.1002/grl.50289>.
- , and Coauthors, 2020: Impact of ocean resolution and mean state on the rate of AMOC weakening. *Climate Dyn.*, **55**, 1711–1732, <https://doi.org/10.1007/s00382-020-05345-9>.
- Jansen, M. F., and L.-P. Nadeau, 2016: The effect of Southern Ocean surface buoyancy loss on the deep-ocean circulation and stratification. *J. Phys. Oceanogr.*, **46**, 3455–3470, <https://doi.org/10.1175/JPO-D-16-0084.1>.
- , and —, 2019: A toy model for the response of the residual overturning circulation to surface warming. *J. Phys. Oceanogr.*, **49**, 1249–1268, <https://doi.org/10.1175/JPO-D-18-0187.1>.
- , —, and T. M. Merlis, 2018: Transient versus equilibrium response of the ocean's overturning circulation to warming. *J. Climate*, **31**, 5147–5163, <https://doi.org/10.1175/JCLI-D-17-0797.1>.
- Kostov, Y., K. C. Armour, and J. Marshall, 2014: Impact of the Atlantic meridional overturning circulation on ocean heat storage and transient climate change. *Geophys. Res. Lett.*, **41**, 2108–2116, <https://doi.org/10.1002/2013GL058998>.
- Krebs, U., and A. Timmermann, 2007: Tropical air–sea interactions accelerate the recovery of the Atlantic meridional overturning circulation after a major shutdown. *J. Climate*, **20**, 4940–4956, <https://doi.org/10.1175/JCLI4296.1>.
- Levang, S. J., and R. W. Schmitt, 2020: What causes the AMOC to weaken in CMIP5? *J. Climate*, **33**, 1535–1545, <https://doi.org/10.1175/JCLI-D-19-0547.1>.
- Lévy, M., P. Klein, A.-M. Tréguier, D. Iovino, G. Madec, S. Masson, and K. Takahashi, 2010: Modifications of gyre circulation by sub-mesoscale physics. *Ocean Modell.*, **34** (1–2), 1–15, <https://doi.org/10.1016/j.oceomod.2010.04.001>.
- Li, H., A. Fedorov, and W. Liu, 2021: AMOC stability and diverging response to Arctic sea ice decline in two climate models. *J. Climate*, **34**, 5443–5460, <https://doi.org/10.1175/JCLI-D-20-0572.1>.
- Liu, W., Z. Liu, and E. C. Brady, 2014: Why is the AMOC monostable in coupled general circulation models? *J. Climate*, **27**, 2427–2443, <https://doi.org/10.1175/JCLI-D-13-00264.1>.
- , S.-P. Xie, Z. Liu, and J. Zhu, 2017: Overlooked possibility of a collapsed Atlantic meridional overturning circulation in warming climate. *Sci. Adv.*, **3**, e1601666, <https://doi.org/10.1126/sciadv.1601666>.
- , A. V. Fedorov, S.-P. Xie, and S. Hu, 2020: Climate impacts of a weakened Atlantic meridional overturning circulation in a warming climate. *Sci. Adv.*, **6**, eaaz4876, <https://doi.org/10.1126/sciadv.aaz4876>.
- Lynch-Stieglitz, J., and Coauthors, 2007: Atlantic meridional overturning circulation during the Last Glacial Maximum. *Science*, **316**, 66–69, <https://doi.org/10.1126/science.1137127>.
- Manabe, S., and R. J. Stouffer, 1994: Multiple-century response of a coupled ocean–atmosphere model to an increase of atmospheric carbon dioxide. *J. Climate*, **7**, 5–23, [https://doi.org/10.1175/1520-0442\(1994\)007<0005:MCROAC>2.0.CO;2](https://doi.org/10.1175/1520-0442(1994)007<0005:MCROAC>2.0.CO;2).
- Maroon, E. A., J. E. Kay, and K. B. Karnauskas, 2018: Influence of the Atlantic meridional overturning circulation on the Northern Hemisphere surface temperature response to radiative forcing. *J. Climate*, **31**, 9207–9224, <https://doi.org/10.1175/JCLI-D-17-0900.1>.
- Marshall, J., A. Donohoe, D. Ferreira, and D. McGee, 2014: The ocean's role in setting the mean position of the Inter-Tropical Convergence Zone. *Climate Dyn.*, **42**, 1967–1979, <https://doi.org/10.1007/s00382-013-1767-z>.
- Mauritsen, T., and Coauthors, 2019: Developments in the MPI-M Earth System Model version 1.2 (MPI-ESM1.2) and its response to increasing CO₂. *J. Adv. Model. Earth Syst.*, **11**, 998–1038, <https://doi.org/10.1029/2018MS001400>.
- McDougall, T. J., and P. M. Barker, 2011: Getting started with TEOS-10 and the Gibbs Seawater (GSW) Oceanographic Toolbox, SCOR/IAPSO WG127, Vol. 37, 28 pp., https://www.teos-10.org/pubs/Getting_Started.pdf.
- Mecking, J., S. S. Drijfhout, L. C. Jackson, and T. Graham, 2016: Stable AMOC off state in an eddy-permitting coupled climate model. *Climate Dyn.*, **47**, 2455–2470, <https://doi.org/10.1007/s00382-016-2975-0>.
- Muglia, J., and A. Schmittner, 2015: Glacial Atlantic overturning increased by wind stress in climate models. *Geophys. Res. Lett.*, **42**, 9862–9868, <https://doi.org/10.1002/2015GL064583>.
- Nadeau, L.-P., and M. F. Jansen, 2020: Overturning circulation pathways in a two-basin ocean model. *J. Phys. Oceanogr.*, **50**, 2105–2122, <https://doi.org/10.1175/JPO-D-20-0034.1>.
- Newsom, E. R., and A. F. Thompson, 2018: Reassessing the role of the Indo-Pacific in the ocean's global overturning circulation. *Geophys. Res. Lett.*, **45**, 12 422–12 431, <https://doi.org/10.1029/2018GL080350>.
- , C. M. Bitz, F. O. Bryan, R. Abernathy, and P. R. Gent, 2016: Southern Ocean deep circulation and heat uptake in a

- high-resolution climate model. *J. Climate*, **29**, 2597–2619, <https://doi.org/10.1175/JCLI-D-15-0513.1>.
- , A. F. Thompson, J. F. Adkins, and E. D. Galbraith, 2021: A hemispheric asymmetry in poleward ocean heat transport across climates: Implications for overturning and polar warming. *Earth Planet. Sci. Lett.*, **568**, 117033, <https://doi.org/10.1016/j.epsl.2021.117033>.
- Nikurashin, M., and G. Vallis, 2012: A theory of the interhemispheric meridional overturning circulation and associated stratification. *J. Phys. Oceanogr.*, **42**, 1652–1667, <https://doi.org/10.1175/JPO-D-11-0189.1>.
- Pithan, F., and T. Jung, 2021: Arctic amplification of precipitation changes—The energy hypothesis. *Geophys. Res. Lett.*, **48**, e2021GL094977, <https://doi.org/10.1029/2021GL094977>.
- Ragen, S., K. C. Armour, L. Thompson, A. Shao, and D. Darr, 2022: The role of Atlantic basin geometry in meridional overturning circulation. *J. Phys. Oceanogr.*, **52**, 475–492, <https://doi.org/10.1175/JPO-D-21-0036.1>.
- Rind, D., G. A. Schmidt, J. Jonas, R. Miller, L. Nazarenko, M. Kelley, and J. Romanski, 2018: Multicentury instability of the Atlantic meridional circulation in rapid warming simulations with GISS ModelE2. *J. Geophys. Res. Atmos.*, **123**, 6331–6355, <https://doi.org/10.1029/2017JD027149>.
- Rugenstein, M. A., J. M. Gregory, N. Schaller, J. Sedláček, and R. Knutti, 2016a: Multiannual ocean–atmosphere adjustments to radiative forcing. *J. Climate*, **29**, 5643–5659, <https://doi.org/10.1175/JCLI-D-16-0312.1>.
- , J. Sedláček, and R. Knutti, 2016b: Nonlinearities in patterns of long-term ocean warming. *Geophys. Res. Lett.*, **43**, 3380–3388, <https://doi.org/10.1002/2016GL068041>.
- , and Coauthors, 2019: LongRunMIP: Motivation and design for a large collection of millennial-length AOGCM simulations. *Bull. Amer. Meteor. Soc.*, **100**, 2551–2570, <https://doi.org/10.1175/BAMS-D-19-0068.1>.
- , and Coauthors, 2020: Equilibrium climate sensitivity estimated by equilibrating climate models. *Geophys. Res. Lett.*, **47**, e2019GL083898, <https://doi.org/10.1029/2019GL083898>.
- Saint-Martin, D., and Coauthors, 2019: Fast-forward to perturbed equilibrium climate. *Geophys. Res. Lett.*, **46**, 8969–8975, <https://doi.org/10.1029/2019GL083031>.
- Schmidt, G. A., and Coauthors, 2014: Configuration and assessment of the GISS ModelE2 contributions to the CMIP5 archive. *J. Adv. Model. Earth Syst.*, **6**, 141–184, <https://doi.org/10.1002/2013MS000265>.
- Schmittner, A., M. Latif, and B. Schneider, 2005: Model projections of the North Atlantic thermohaline circulation for the 21st century assessed by observations. *Geophys. Res. Lett.*, **32**, L23710, <https://doi.org/10.1029/2005GL024368>.
- Sévellec, F., A. V. Fedorov, and W. Liu, 2017: Arctic sea-ice decline weakens the Atlantic meridional overturning circulation. *Nat. Climate Change*, **7**, 604–610, <https://doi.org/10.1038/nclimate3353>.
- Sigmond, M., J. C. Fyfe, O. A. Saenko, and N. C. Swart, 2020: Ongoing AMOC and related sea-level and temperature changes after achieving the Paris targets. *Nat. Climate Change*, **10**, 672–677, <https://doi.org/10.1038/s41558-020-0786-0>.
- Speer, K., and E. Tziperman, 1992: Rates of water mass formation in the North Atlantic Ocean. *J. Phys. Oceanogr.*, **22**, 93–104, [https://doi.org/10.1175/1520-0485\(1992\)022<0093:ROWMFI>2.0.CO;2](https://doi.org/10.1175/1520-0485(1992)022<0093:ROWMFI>2.0.CO;2).
- Stocker, T. F., and A. Schmittner, 1997: Influence of CO₂ emission rates on the stability of the thermohaline circulation. *Nature*, **388**, 862–865, <https://doi.org/10.1038/42224>.
- Stommel, H., 1961: Thermohaline convection with two stable regimes of flow. *Tellus*, **13**, 224–230, <https://doi.org/10.3402/tellusa.v13i2.9491>.
- Stouffer, R. J., and S. Manabe, 2003: Equilibrium response of thermohaline circulation to large changes in atmospheric CO₂ concentration. *Climate Dyn.*, **20**, 759–773, <https://doi.org/10.1007/s00382-002-0302-4>.
- , and Coauthors, 2006: Investigating the causes of the response of the thermohaline circulation to past and future climate changes. *J. Climate*, **19**, 1365–1387, <https://doi.org/10.1175/JCLI3689.1>.
- Sun, S., I. Eisenman, and A. L. Stewart, 2018: Does Southern Ocean surface forcing shape the global ocean overturning circulation? *Geophys. Res. Lett.*, **45**, 2413–2423, <https://doi.org/10.1002/2017GL076437>.
- , —, L. Zanna, and A. L. Stewart, 2020a: Surface constraints on the depth of the Atlantic meridional overturning circulation: Southern Ocean versus North Atlantic. *J. Climate*, **33**, 3125–3149, <https://doi.org/10.1175/JCLI-D-19-0546.1>.
- , A. F. Thompson, and I. Eisenman, 2020b: Transient overturning compensation between Atlantic and Indo-Pacific basins. *J. Phys. Oceanogr.*, **50**, 2151–2172, <https://doi.org/10.1175/JPO-D-20-0060.1>.
- , —, S.-P. Xie, and S.-M. Long, 2022: Indo-Pacific warming induced by a weakening of the Atlantic meridional overturning circulation. *J. Climate*, **35**, 815–832, <https://doi.org/10.1175/JCLI-D-21-0346.1>.
- Thomas, M. D., and A. V. Fedorov, 2019: Mechanisms and impacts of a partial AMOC recovery under enhanced freshwater forcing. *Geophys. Res. Lett.*, **46**, 3308–3316, <https://doi.org/10.1029/2018GL080442>.
- Thorpe, R., J. M. Gregory, T. Johns, R. Wood, and J. Mitchell, 2001: Mechanisms determining the Atlantic thermohaline circulation response to greenhouse gas forcing in a non-flux-adjusted coupled climate model. *J. Climate*, **14**, 3102–3116, [https://doi.org/10.1175/1520-0442\(2001\)014<3102:MDTATC>2.0.CO;2](https://doi.org/10.1175/1520-0442(2001)014<3102:MDTATC>2.0.CO;2).
- Vellinga, M., R. A. Wood, and J. M. Gregory, 2002: Processes governing the recovery of a perturbed thermohaline circulation in HadCM3. *J. Climate*, **15**, 764–780, [https://doi.org/10.1175/1520-0442\(2002\)015<0764:PGTROA>2.0.CO;2](https://doi.org/10.1175/1520-0442(2002)015<0764:PGTROA>2.0.CO;2).
- Walín, G., 1982: On the relation between sea-surface heat flow and thermal circulation in the ocean. *Tellus*, **34**, 187–195, <https://doi.org/10.3402/tellusa.v34i2.10801>.
- Weaver, A. J., M. Eby, M. Kienast, and O. A. Saenko, 2007: Response of the Atlantic meridional overturning circulation to increasing atmospheric CO₂: Sensitivity to mean climate state. *Geophys. Res. Lett.*, **34**, L05708, <https://doi.org/10.1029/2006GL028756>.
- Weber, S., and Coauthors, 2007: The modern and glacial overturning circulation in the Atlantic Ocean in PMIP coupled model simulations. *Climate Past*, **3**, 51–64, <https://doi.org/10.5194/cp-3-51-2007>.
- Weijer, W., W. Cheng, O. A. Garuba, A. Hu, and B. T. Nadiga, 2020: CMIP6 models predict significant 21st century decline of the Atlantic meridional overturning circulation. *Geophys. Res. Lett.*, **47**, e2019GL086075, <https://doi.org/10.1029/2019GL086075>.
- Welander, P., 1971: A discussion on ocean currents and their dynamics—The thermocline problem. *Philos. Trans. Roy. Soc.*, **A270**, 415–421, <https://doi.org/10.1098/rsta.1971.0081>.

- Wiebe, E., and A. Weaver, 1999: On the sensitivity of global warming experiments to the parametrisation of sub-grid scale ocean mixing. *Climate Dyn.*, **15**, 875–893, <https://doi.org/10.1007/s003820050319>.
- Wolfe, C. L., and P. Cessi, 2010: What sets the strength of the middepth stratification and overturning circulation in eddy ocean models? *J. Phys. Oceanogr.*, **40**, 1520–1538, <https://doi.org/10.1175/2010JPO4393.1>.
- Wu, P., L. Jackson, A. Pardaens, and N. Schaller, 2011: Extended warming of the northern high latitudes due to an overshoot of the Atlantic meridional overturning circulation. *Geophys. Res. Lett.*, **38**, L24704, <https://doi.org/10.1029/2011GL049998>.
- Yin, J., and R. J. Stouffer, 2007: Comparison of the stability of the Atlantic thermohaline circulation in two coupled atmosphere–ocean general circulation models. *J. Climate*, **20**, 4293–4315, <https://doi.org/10.1175/JCLI4256.1>.
- Zhu, C., and Z. Liu, 2020: Weakening Atlantic overturning circulation causes South Atlantic salinity pile-up. *Nat. Climate Change*, **10**, 998–1003, <https://doi.org/10.1038/s41558-020-0897-7>.
- Zhu, J., Z. Liu, X. Zhang, I. Eisenman, and W. Liu, 2014: Linear weakening of the AMOC in response to receding glacial ice sheets in CCSM3. *Geophys. Res. Lett.*, **41**, 6252–6258, <https://doi.org/10.1002/2014GL060891>.
- , —, J. Zhang, and W. Liu, 2015: AMOC response to global warming: Dependence on the background climate and response timescale. *Climate Dyn.*, **44**, 3449–3468, <https://doi.org/10.1007/s00382-014-2165-x>.